

General Disclaimer

One or more of the Following Statements may affect this Document

- This document has been reproduced from the best copy furnished by the organizational source. It is being released in the interest of making available as much information as possible.
- This document may contain data, which exceeds the sheet parameters. It was furnished in this condition by the organizational source and is the best copy available.
- This document may contain tone-on-tone or color graphs, charts and/or pictures, which have been reproduced in black and white.
- This document is paginated as submitted by the original source.
- Portions of this document are not fully legible due to the historical nature of some of the material. However, it is the best reproduction available from the original submission.

FINAL PROGRESS REPORT

TO: National Aeronautics and Space Administration
Office of Space and Terrestrial Applications
Goddard Space Flight Center
Laboratory for Atmospheric Sciences

REFERENCE: NASA Grant No.: NAG 5-107

ORGANIZATION: Center for Climatic Research
Department of Geography
University of Delaware
Newark, DE 19716



PROJECT TITLE: A Climatically-Derived Global Soil
Moisture Data Set for Use in the
GLAS Atmospheric Circulation Model
Seasonal Cycle Experiment

PERSONNEL

Project Director: Dr. John R. Mather
Principal Investigator: Dr. Cort J. Willmott
Co-Investigatior: Mr. Richard T. Field

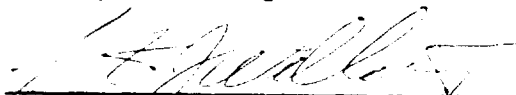
DATE: February 1, 1984

TIME PERIOD: Three Years, September 1980 - June 1983

BUDGET:

SIGNATURE

Principal Investigator:


Cort J. Willmott

(NASA-CR-173289) A CLIMATICALLY-DERIVED
GLOBAL SOIL MOISTURE DATA SET FOR USE IN THE
GLAS ATMOSPHERIC CIRCULATION MODEL SEASONAL
CYCLE EXPERIMENT Final Progress Report,
Sep. 1980 - Jun. 1983 (Delaware Univ.)

N84-17729

Uncias
G3/46 18319

INTRODUCTION

The main tasks outlined in our original proposal to NASA "A Climatically-Derived Global Soil Moisture Data Set for Use in the GLAS Atmospheric Circulation Model Seasonal Cycle Experiment" included:

1. The estimation of monthly, terrestrial soil moisture (w) fields at a resolution of 1° of latitude by 1° of longitude.
2. The estimation and mapping (for verification purposes) of monthly potential evapotranspiration (E_m^o), actual evapotranspiration (E_m), water surplus (Δw), air temperature (T_m) and precipitation (P_m). These fields also were to have a $1^\circ \times 1^\circ$ resolution.
3. The evaluation of Thornthwaite's E_m^o function in areas where it is thought to yield inaccurate estimates, e.g., in monsoonal and arctic environments. At the same time, the function which represents the resistance of the soil-plant system to E_m^o (β) was to be investigated.
4. The final phase of the research was to be a comparison between the GLAS GCM-generated water balance and our Thornthwaite-based water balance.

During the course of our research, the focus of our efforts evolved in response to unanticipated findings as well as to discussions with Yale Mintz and J. Shukla (the grant monitor) concerning NASA's changing requirements for soil moisture data sets. These considerations ultimately caused us to abandon any effort to complete Task 4, for example, while we undertook a number of additional efforts. These additional tasks included the development of a global snow water equivalent data set as well as an algorithm which could efficiently and accurately interpolate from irregularly spaced station data to the nodes of a regular GCM-compatible lattice. Throughout our work, however, our overriding goal of estimating realistic monthly soil moisture values for the globe remained unaltered. Below we briefly describe our grant-related accomplishments. Much of this work also was discussed by Willmott (1982) at NASA's Climate Science Review as well as in previous progress reports.

DATA SET COMPILATION

Using average monthly air temperature and precipitation data previously compiled by C. W. Thornthwaite and associates, we created a digitally encoded global climate data base. The Thornthwaite data were edited and augmented such that our final data base contains 13,332 station records of monthly air temperature and precipitation as well as ancillary station information such as elevation, longitude and latitude. Willmott et al. (1981) published the data and a magnetic tape copy of the data plus documentation were made available to NASA's Goddard Laboratory for Atmospheric Science. The details concerning these data were not only described by Willmott et al. (1981) but they were discussed in the second and third progress reports.

ALGORITHM DEVELOPMENT

When our proposal was written, neither ourselves or NASA personnel were aware that snow could not be adequately treated by our proposed water budget procedure. We further did not anticipate that adequate means were not available to interpolate values from the irregularly spaced stations to the grid points of a GCM-compatible lattice. Mapping procedures that were available, including the one we had proposed to employ (SYMAP), produced an unacceptable interpolation error because the interpolation computations were performed in a projected, Cartesian space. Our solutions to these problems, i.e., the development of new algorithms to include a snow budget in our water budget calculations and to interpolate and contour data in spherical space, are discussed by Willmott et al. (1984a) and Willmott et al. (1984b) (Appendix 1 and 2) as well as in the first, second and third progress reports.

EVALUATION OF THE THORNTHWAITE

WATER BUDGET

Evaluations of the Thornthwaite water budget were made by comparing (1) lysimeter-derived E_m^O estimates with E_m^O values predicted by the Thornthwaite model and (2) measured runoff, runoff predicted by one of Lettau's formulations and runoff derived from the Thornthwaite water balance (Appendix 3). The withdrawal function (β) was also investigated through sensitivity analysis (Willmott and Rowe, 1981) and evaluation with a modicum of published measurements.

Comparisons between observed (lysimeter-derived) E_m^O and Thornthwaite-predicted E_m^O were inconclusive although scientific interpretation of results suggests that Thornthwaite's E_m^O values are more representative of regional E_m^O than commonly believed. Aspects of these comparisons are given by Willmott (1984) and they also are discussed in the third progress report. Evaluations of runoff predictions using measurements and Lettau's model were made by the Co-investigator, Richard Field, and his findings were similarly inconclusive (see Appendix 3).

Plant-soil conductance to evapotranspiration is normally specified as a function of the ratio of soil moisture to field capacity (w/w_*). This function is often referred to as the 'beta function' where $\beta = f(w/w_*)$. Willmott and Rowe (1981) found that the African seasonal soil moisture cycle, particularly in sub-Saharan Africa, was highly sensitive to the selection of the β -function and their results are briefly outlined in the first progress report. Further research indicated that a β -function suggested by Nappo (1975), when used in conjunction with a field capacity of 150 mm, would give reasonable soil moisture

and evapotranspiration estimates for much of the globe. Nappo's (1975) β -function was subsequently employed in the global water budget analysis presented by Willmott et al. (1984b).

ESTIMATED MONTHLY CLIMATE FIELDS

Using the above-described air temperature and precipitation data set, and our water balance and mapping procedures, we derived monthly GCM-compatible fields of air temperature (T_m), precipitation (P_m), potential evapotranspiration (E_m^0), actual evapotranspiration (E_m), snow cover water equivalent (w_m^s) and soil moisture (w_m) at each of the 13,332 station locations. Values of these variables then were interpolated to the nodes of a 1° of latitude by 1° of longitude lattice and visual verification (maps) of T_m , P_m , w_m and w_m^s were presented in the fourth progress report. A magnetic tape copy of the monthly fields of T_m , P_m , E_m^0 , E_m , w_m and w_m^s was made available to NASA's Laboratory of Atmospheric Science. These data sets were further evaluated and described by Willmott et al. (1984b) and their creation marks the successful completion of the main task associated with our grant. An additional global water balance was computed from 899 of the World Weather Records stations (at J. Shukla's request) and those fields also were magnetically encoded and given to the Laboratory of Atmospheric Science. This six-year (1974-1979) calculation is described in the third progress report.

ONGOING RESEARCH

Our research into the global water budget in part suggested that increased levels of biophysical realism should be incorporated into GCM-representations of the near-surface hydrology. The Principal Investigator with Yale Mintz and Piers Sellers of NASA subsequently requested and received funding from NSF and

NASA to develop a model biosphere for use in GCM's (Mintz et al. 1983). We are about six months into this research and we will likely use the above-described data sets in the evaluation of our proposed biosphere model; that is, to see if our biosphere model improves GCM-predictions of near-surface hydrological cycle.

PUBLICATIONS AND PAPERS¹

- *Mintz, Y., P. J. Sellers and C. J. Willmott. On the Design of an Interactive Biosphere for the GLAS General Circulation Model. Greenbelt, MD: Goddard Space Flight Center, Laboratory for Atmospheric Sciences, Modeling and Simulation Facility, 1983 (NASA Tech. Memo. 84973).
- *Nappo, C. J. "Parameterization of Surface Moisture and Evaporation Rate in a Planetary Boundary Layer Model." J. of Applied Meteorology. 14 (1975) 289-296.
- Rowe, C. M. and C. J. Willmott. "Sensitivity of Isoline Positions on Small-scale Maps to Some Common Assumptions and Methods of Digital Interpolation." Paper presented at the Annual Meeting of the Middle States Division of the Association of American Geographers, Rochester, New York, October 1981.
- *Willmott, C. J. WATBUG: A FORTRAN IV Algorithm for Calculating the Climatic Water Budget. Elmer, N.J.: C. W. Thornthwaite, Laboratory of Climatology, 1977 (Pubs. in Climatology, XXX, No. 2). Also published as Report 1 in The Use of the Climatic Water Budget in Water Resources Management and Control. Newark, DE.: Univ. of Delaware, Water Resources Center.
- Willmott, C. J. "Zeroth-order Approximation of Global Soil Moisture for Use in the GLAS General Circulation Model." Climate Science Review, NASA, Goddard Space Flight Center, Greenbelt, Maryland, June 1982.
- *Willmott, C. J. "On the Evaluation of Model Performance in Physical Geography" in G. Gaile and C. Willmott (eds). Spatial Statistics and Models. Dordrecht, Holland: D. Reidel. 1984, 443-460.
- Willmott, C. J., J. R. Mather and C. M. Rowe. Average Monthly and Annual Surface Air Temperature and Precipitation Data for the World. Part 1 the Eastern Hemisphere. Part 2 - the Western Hemisphere. Elmer, N.J.: C. W. Thornthwaite, Laboratory of Climatology, 1981 (Pubs. in Climatology, XXXIV, Nos. 1 and 2).

Willmott, C. J. and C. M. Rowe. "Sensitivity of the Climatic Water Budget to Key Boundary Conditions and Parameterizations." Paper presented at the Annual Meeting of the Association of American Geographers, Los Angeles, California, April 1981.

Willmott, C. J., C. M. Rowe and F. Gossette. "Small-scale Isoline Maps: Some Projection-related Inaccuracies Resulting from Interpolation in Cartesian Space." Paper presented at the Annual Meeting of the Association of American Geographers, San Antonio, Texas, April 1982.

Willmott, C. J., C. M. Rowe and W. D. Philpot. "Small-scale Climate Maps: A Sensitivity Analysis of Some Common Assumptions Associated with Grid Point Interpolation and Contouring." American Cartographer. 1984a accepted for publication.

Willmott, C. J., C. M. Rowe and Y. Mintz. "An Empirically-Derived Climatology of the Terrestrial Seasonal Water Cycle." J. of Climatology. 1984b, in preparation.

¹Publications which did not arise directly from grant-related tasks are starred.

APPENDIX 1

**Small-scale Climate Maps: A Sensitivity Analysis
of Some Common Assumptions Associated with Grid
Point Interpolation and Contouring.**

**Small-scale Climate Maps: A Sensitivity Analysis of Some Common
Assumptions Associated with Grid Point Interpolation and
Contouring**

by

One Ft

Cort J. Willmott

Clinton M. Rowe

Center for Climatic Research
Department of Geography
University of Delaware
Newark, Delaware 19711

and

William D. Philpot

Remote Sensing Program
School of Civil and Environmental Engineering
Cornell University
Ithaca, New York 14853

with 4 figures

1984
~~September 1983~~

Abstract

Algorithms for point interpolation and contouring on the surface of the sphere and in Cartesian two-space are developed from Shepard's (1968) well-known, local-search method. These mapping procedures then are used to investigate the errors which appear on small-scale climate maps as a result of the all-too-common practice of interpolating — from irregularly spaced data points to the nodes of a regular lattice — and contouring in Cartesian two-space. Using mean annual air temperatures drawn from 100 irregularly spaced weather stations, the annual air temperature field over the western half of the northern hemisphere is estimated both on the sphere — assumed to be correct — and in Cartesian two-space. When the spherically- and Cartesian-approximated air temperature fields are mapped and compared, the magnitudes (as large as 5° to 10°C) and distribution of the errors associated with the latter approach become apparent.

Key Words

Climate, mapping, interpolation, contouring

Introduction

Within climatology, automated point interpolation and isoline construction have widely replaced the relatively subjective methods of their draftsman predecessors. Cartographers have provided us with numerous digital algorithms for solving the typical problems associated with interpolating from irregularly spaced data points in Cartesian two-space to the nodes of a regular lattice and isoline placement among the estimated grid point values (Peucker 1980; Rhind 1975; Morrison 1974; Marble 1981). It is possible, but uncommon in climatology, to draw isolines directly from the irregularly spaced data, ostensibly because the grid point values frequently are required for subsequent analyses.

Another source of potentially useful interpolation and contouring procedures has been the atmospheric sciences where a wide variety of methods have been developed under the rubric of "objective analysis" (Panofsky 1949; Cressman 1959; Barnes 1964; Fritsch 1971; Gandin 1963; Schlatter, *et al.* 1976; Wahba and Wendelberger 1980). In many ways, the development of objective analysis parallels the advancements in cartographic interpolation and contouring except that the impetus for and direction of objective analytic research largely have been determined by the requirements of the weather forecasting community. Objective analysis, as a result, characteristically relies upon the typically smooth nature of upper air data as well as upon multivariate and/or autocorrelative relationships beyond those contained in the irregularly spaced scalar field associated with a single variable. Many objective functions, for these reasons, may be inappropriate for mapping the characteristically uneven scalar fields associated with near-surface climate although the objective analysis literature contains a number of innovative approaches to interpolation (e.g., Wahba 1979, 1981;

Wahba and Wendelberger 1980).

It is important to note that most objective functions, similar to interpolation and contouring procedures developed by cartographers, tacitly assume that the data values have been projected into Cartesian two-space (e.g., Wahba and Wendelberger 1980). Only in a minority of instances have the true relationships between the data and grid points on the surface of the Earth or sphere been preserved and explicitly incorporated into an objective algorithm (e.g., Wahba 1979, 1981).

Point interpolation and isoline construction in climatology characteristically begin with the collection of data values associated with an irregularly distributed set of points on the surface of the Earth. For most climatological purposes, the Earth can be assumed to be a perfect sphere, with a trivial loss of accuracy, and each data observation (subscript i) of the variable of interest, $z_i(\lambda, \phi)$, can be uniquely located by simple longitude (λ) and latitude (ϕ) coordinates. Once the data points have been compiled, they usually are projected into a Cartesian two-space so that each $z_i(\lambda, \phi)$ becomes $z_i(x, y)$, and one of the readily available Cartesian-based interpolation and contouring algorithms (e.g., Marble 1981) may be applied to the data. Many times the projection is indirectly accomplished by the estimation of x and y from an existing map or by the scaled, but otherwise unaltered, assignment of λ and $\phi + \pi$ and y , respectively. Estimates of $z_j(x, y)$ then are made at the nodes (subscript j) of a regular lattice by point interpolation, which is ordinarily followed by the lacing of isolines through the lattice of interpolated values. During contour lacing, the points — grid points in this case — once again are assumed to be correctly related by the projected Cartesian geometry. Assumed Cartesian relationships between the projected points,

in other words, underlies the interpolation of grid point values and often contributes twice to the estimation of isoline locations.

When mapping climate fields that extend over large areas of the Earth's surface, however, it is well known that spherical distance and/or directional relationships cannot be accurately preserved in the translation to Cartesian two-space. Subsequent interpolation and contouring — based on the projected relationships — will necessarily be in error. The magnitude of the errors, of course, will completely depend on the map projection selected, the distribution of the data and grid points, and the properties of the interpolation and contouring algorithm. It will be shown that this error can be marked.

In order to avoid the propagation of such errors in small-scale mapping, climatologists should perform their interpolation and contouring on the surface of the sphere, i.e., in "spherical space". That is, the interpolation and contouring processes should depend only upon the spherical geometry that relates the grid and data points on the Earth's surface. Only after the grid point values and contour positions have been determined on the sphere should they be projected onto a map.

Even though most climatological papers do not describe or even cite the interpolation and/or contouring methods from which their climate maps were generated, errors that are derivative from the Cartesian-based interpolations are commonplace within the literature. Any of the numerous SYMAP (Shepard 1968), IMSL (Akima 1978) or SURFACE II (Sampson 1978) computed contour maps, for example, assume a Cartesian space. On any given small-scale climate map, particularly when the algorithm is not described, the nature and degree of error may be difficult to ascertain. In

cases where the mapped area extends to one or more of the poles or over all 360 degrees of longitude, however, two symptoms can easily be recognized. Cylindrical projections which have as their edges the north or south poles and the dateline, for instance, typically exhibit 1) multiple isolines crossing the poles and/or 2) contours which do not meet at the dateline (e.g., Schlatter, *et al.* 1976; Halem, *et al.* 1982; Rivin and Kulikov 1982). Suffice it to say that consideration of interpolation and/or contouring errors produced by the projection of data points into Cartesian space prior to grid point interpolation and contouring largely has been overlooked by climatologists.

In order to examine the degree to which Cartesian-based interpolation and contouring can ill-effect the small-scale mapping and analysis of climate fields, we present the results of two sets of map-analyses based upon two modified versions of Shepard's (1968) interpolation algorithm. These procedures also were augmented by two contouring routines in order to permit the plotting of isolines. Shepard's (1968) function was selected as a benchmark procedure because of its wide-spread use (e.g., by 1980 — in the form of SYMAP — it was implemented at well over 500 organizations) and because it represents a class of point interpolation algorithms that have an intuitive appeal (Shepard 1968) and are "relatively robust" (Rhind 1975:299).

Our first implementation of Shepard's method is quite similar to that of SYMAP in as much as all interpolations and isoline determinations assume that the data and grid points are correctly related in Cartesian two-space. Our second, "spherically-based" version computes all interpolations and isoline positions from the actual data and grid point locations on the surface of the sphere. Longitude and latitude coordinates associated with each spherically-derived isoline are then projected along with all

other substantive elements of the map onto a Cartesian two-space.

Following descriptions of these two algorithms — with an emphasis on the spherically-based procedures which have not been discussed previously — we describe results obtained from comparative mappings of an average annual air temperature field which was sampled from a recently compiled world climate data set (Willmott, *et al.* 1981). Our two implementations of Shepard's (1968) function are described in the next section of this paper followed by an examination of two air temperature maps which were derived from combinations of the above-mentioned air temperature field, two well-known cylindrical projections and our two interpolation and contouring algorithms.

Grid Point Interpolation

Shepard's (1968) interpolation function estimates a value at each node of a predetermined lattice from a small number of nearby data points. Developed for interpolation within Cartesian two-space, the procedure accounts for the distance and directional relationships between neighboring data and grid points (Figure 1). The algorithm also has a limited extrapolation capability that permits grid points to take on values outside the range of the data. Although there are a few important differences between the algorithms described here and Shepard's (1968) original function, the essence of his function has been maintained.

Based upon a simple gravity hypothesis and other considerations (Shepard 1968, 1983), the interpolation procedure requires that the value of each nearby data point influence the estimation of the associated grid point value by an amount proportional to their distance from one another. Weights are ascribed to three categories of

distance according to

$$S_k = \begin{cases} d_{j,k}^{-1} & d_{j,k} \leq r_j/3 \\ \frac{27}{4r_j} \left(\frac{d_{j,k}}{r_j} - 1 \right)^2 & r_j/3 < d_{j,k} \leq r_j \\ 0 & d_{j,k} > r_j \end{cases} \quad (1)$$

where r_j is the search radius (defined below) and $d_{j,k}$ is the distance from grid point j to nearby data point k . The subscript k (and later l) is used to reference one of those data points near j which belongs to the set of data points that influence the interpolated value at j . Following Shepard (1968), the search radius is initially defined as a constant, i.e., as the radius of a circle (on either the plane or the sphere) which contains seven data points — on the average. In cases where less than four or more than 10 data points fall within r_j of j , r_j is adjusted. When the former occurs, r_j is set equal to the distance of the fifth closest data point while, in the latter case, r_j is redefined as the distance to the eleventh nearest data point. Four or 10 data points then will lie within the circle (area) of influence represented by the adjusted search radius. Each grid point value thus represents a constant area of influence — except when fewer than four or more than 10 data points fall within the initial search radius — and from four to 10 data values.

For each grid point, in other words, two sets of n_j ($4 \leq n_j \leq 10$) nearby data points are selected; one set on the basis of their Cartesian distances from j in the projected two-space and the other on the basis of their distances from j on the surface of the sphere. On the sphere (Figure 1a), $d_{j,k}^s$ — the great circle distance between points j and k — is obtained from

$$\cos d_{j,k}^s = \sin \phi_j \sin \phi_k + \cos \phi_j \cos \phi_k \cos (\lambda_j - \lambda_k) \quad (2a)$$

whereas Cartesian distance (Figure 1b) is computed from the well-known rectangular distance formula

$$d_{j,k}^c = \left[(x_k - x_j)^2 + (y_k - y_j)^2 \right]^{0.5} \quad (2b)$$

It should be noted that the superscripts *c* and *s*, respectively, are used to distinguish Cartesian- from spherically-derived distances and angles. When a distance or angle appears without a superscript, it represents either system of geometry. Each set of n_j nearest neighbors then is sorted in ascending order which provides that $d_{j,1}$ and d_{j,n_j} are associated with the nearby data points of minimum and maximum distance from *j*, respectively.

Once $(S_k, k=1, n_j)$ have been computed (1), Shepard's function corrects for the "directional isolation" of each data point relative to all the other nearby data points. Although a few authors (Morrison 1974) have suggested that such adjustments may be inconsequential or even deleterious to the accurate reproduction of a known functionally-derived surface, such a correction makes theoretical sense (Shepard 1983). Directional isolation of each nearby data point with regard to *j* is computed from

$$T_k = \sum_{l=1}^{n_j} S_l \left[1 - \cos \theta_j(k,l) \right], \quad l \neq k \quad (3)$$

where $\theta_j(k,l)$ is the angular separation of nearby data points *k* and *l* when the vertex of the angle is defined as grid point *j* (Figure 1). The angular solitude of a data point with respect to *j* — on the sphere — is derived from

$$\cos \theta_j^s(k,l) = (\cos d_{k,l}^s - \cos d_{j,k}^s \cos d_{j,l}^s) (\sin d_{j,k}^s \sin d_{j,l}^s)^{-1} \quad l \neq k \quad (4a)$$

For points projected into Cartesian space, the separation is obtained from the definition of the angle between two vectors; that is,

$$\cos \theta_j^c(k,l) = \frac{(x_k - x_j)(x_l - x_j) + (y_k - y_j)(y_l - y_j)}{d_{j,k}^c d_{j,l}^c} \quad l \neq k \quad (4b)$$

Thus, data points that have a small angular separation contribute less individually than points which have a large angular separation. With the directional isolation of data point k known, a combined set of weights is calculated from

$$W_k = S_k^2 \left(1 + T_k / \sum_{l=1}^{n_j} S_l \right) \quad l \neq k \quad (5)$$

which limits the maximum influence of the directional isolation of k to a doubling of the weight based on distance (Shepard 1983), i.e., when $T_k = \sum_{l=1}^{n_j} S_l$.

In order to obtain non-zero gradients on the interpolated surface at data points, increments (Δz_k) are computed and added to the respective data point values (z_k). The correction involves finding an average weighted gradient for each of the n_j data points within r_j of j , based upon the collective rates of change at the other data points within r_j . On the surface of the sphere, the incremental corrections are obtained for each of the data points associated with j from

$$\Delta z_k = \left\{ \frac{\partial(\overline{\Delta z})}{\partial \lambda} \right\}_k d_\lambda^s(j,k) + \left\{ \frac{\partial(\overline{\Delta z})}{\partial \phi} \right\}_k d_\phi^s(j,k) \left\{ v / (v + d_{j,k}^s) \right\} \quad (6)$$

where $\partial(\overline{\Delta z})/\partial \lambda$ is the average partial derivative with respect to longitude, $\partial(\overline{\Delta z})/\partial \phi$ is the average partial derivative with respect to latitude, $d_\lambda^s(j,k) = (\lambda_j - \lambda_k) \cos \phi_j$ and $d_\phi^s(j,k) = \phi_j - \phi_k$. The average partial derivatives are taken as

$$\left. \frac{\partial(\Delta z)}{\partial \lambda} \right|_k = \frac{\sum_{l=1}^{n_j} W_l(z_l - z_k) d_\lambda^s(l, k) d_{k,l}^s{}^{-2}}{\sum_{l=1}^{n_j} W_l} \quad l \neq k \quad (7a)$$

and

$$\left. \frac{\partial(\Delta z)}{\partial \phi} \right|_k = \frac{\sum_{l=1}^{n_j} W_l(z_l - z_k) d_\phi^s(l, k) d_{k,l}^s{}^{-2}}{\sum_{l=1}^{n_j} W_l} \quad l \neq k \quad (7b)$$

where $d_\lambda^s(l, k) = (\lambda_l - \lambda_k) \cos \phi_k$ and $d_\phi^s(l, k) = \phi_l - \phi_k$, while a somewhat arbitrary adjustment is made in order to limit the influence of the increments to one-tenth the data range; that is, so $|\Delta z_k|$ cannot exceed $0.1(\max z_i - \min z_i)$ where again i refers to any data point on the map. Although it is not obvious, the limit of $|\Delta z_k|$ can be deduced from equation (6) by making use of the Cauchy-Schwarz inequality. The adjustment parameter (v) takes the form

$$v = 0.1(\max z_i - \min z_i) \max \left[\left(\left. \frac{\partial(\Delta z)}{\partial \lambda} \right|_k \right)^2 + \left(\left. \frac{\partial(\Delta z)}{\partial \phi} \right|_k \right)^2 \right]^{-0.5} \quad (8)$$

Forms of (6), (7) and (8) also are used for the Cartesian-based computations with $\overline{\partial \Delta z} / \partial x$, $d_x^c(j, k)$, $\overline{\partial \Delta z} / \partial y$, $d_y^c(j, k)$, d_x^c , d_y^c , $d_x^c(l, k)$, $d_y^c(l, k)$ and $d_{k,l}^c$ replacing $\overline{\partial \Delta z} / \partial \lambda$, $d_\lambda^s(j, k)$, $\overline{\partial \Delta z} / \partial \phi$, $d_\phi^s(j, k)$, d_λ^s , d_ϕ^s , $d_\lambda^s(l, k)$, $d_\phi^s(l, k)$ and $d_{k,l}^s$, respectively.

With the evaluation of the above described functions, the value predicted at grid point j (\hat{z}_j) becomes

$$\hat{z}_j = \begin{cases} \frac{\sum_{k=1}^{n_j} W_k(z_k + \Delta z_k) / \sum_{k=1}^{n_j} W_k}{m^{-1} \sum_{k=1}^m z_k} & d_{j,1} > \epsilon \\ m^{-1} \sum_{k=1}^m z_k & d_{j,1} \leq \epsilon \end{cases} \quad (9)$$

where m is the number of data points within ϵ (defined below) of grid point j . That is to say, when one or more data points are sufficiently close to a grid point (i.e., within ϵ of j), the grid point takes on their average value; otherwise, part one of (9) defines the interpolation function. On the surface of the sphere, ϵ is specified as the maximum of a function of 1) the grid cell longitudinal difference ($\Delta\lambda$) and the latitudinal range of the grid points, or 2) the grid cell latitudinal difference ($\Delta\phi$); that is

$$\epsilon^s = \begin{cases} 0.01 \max\{0.5\Delta\lambda[\cos(\max\phi_j) + \cos(\min\phi_j)], \Delta\phi\} & (\max\phi_j)(\min\phi_j) \geq 0.0 \\ 0.01 \max\{0.5\Delta\lambda[\cos(\max|\phi_j|) + 1], \Delta\phi\} & (\max\phi_j)(\min\phi_j) < 0.0 \end{cases} \quad (10a)$$

where $\max\phi_j$ and $\min\phi_j$ are the largest and smallest latitudes, respectively, found among all the grid points and $\max|\phi_j|$ is the grid latitude of greatest magnitude. In other words, when the grid points lie entirely within either the northern or southern hemisphere, ϵ^s is computed from part one of (10a) whereas part two of (10a) is evaluated if the grid spans the equator. For points in Cartesian two-space,

$$\epsilon^c = 0.01 \max(\Delta x, \Delta y) \quad (10b)$$

where Δx is the width and Δy is the height of a typical rectangular grid cell. Using these modified versions of Shepard's (1968) algorithm, point interpolations from irregularly spaced data points can be performed for any bounded rectangular or spherical lattice as well as for any spherical grid that spans the surface of the globe.

Isoline Construction

Once data values have been estimated at all nodes of a lattice, it becomes necessary to describe the gridded data field by fitting and subsequently plotting isolines. Cartesian-based methods of contour-lacing are well-known (e.g., see McCullagh 1981) but a spherically-based lacing routine also was needed in order to position the isolines

on the surface of the sphere and, thereby, not contaminate the presentation of a spherically interpolated field with a projection-related lacing error.

Our primary lacing unit is either a spherical ($\Delta\lambda$ by $\Delta\phi$) or Cartesian (Δx by Δy) grid cell which has its vertices defined by four grid points (Figure 2). Each grid cell is quartered by the definition of a grid cell "center" and the construction of "half-diagonals" which extend from each of the grid cell corners to the center. On the sphere, the center is located at the average latitude and longitude of the cell, while the half-diagonals are the arcs of great circles. In Cartesian two-space, however, the center and half-diagonals are defined by the intersection of the diagonals of a grid quadrilateral (cell) which has as its vertices four projected grid points. Within each spherical or Cartesian grid cell, four triangles are thus created. At the vertex which is shared by the four triangles (the cell center), a value is estimated as the arithmetic mean of the four corner values although this can be a source of error. When the cell-size is relatively small, however — as is the case with the maps discussed in the next section — the error is insignificant. On the other hand, when the lattice is coarse, the center point and its associated value should be more accurately determined. With the definition of a triangular mesh and estimation of center point values, all desired isolines can be unambiguously positioned within the interpolated scalar field.

From an initial point on or intersection with the edge of a first triangle, an isoline must pass through the triangle and intersect one of the two opposite sides at a point determined by the relative magnitudes of the values associated with the end-points of the intersected edge. The coordinates of each intersection are recorded. As the second intersection positions the isoline on an edge of a triangle adjacent to the first, the process may be repeated for the second triangle such that the coordinates of a

third intersection are stored. Then a third triangle adjacent to the second may be evaluated and so on until the isoline either crosses a map boundary or closes itself. By successively reproducing these calculations for the desired number of contour levels, a complete isoline representation of the gridded data field can be computed and stored.

From the series of intersection coordinates associated with the desired isolines, Cartesian-derived contour lines merely have to be scaled and plotted — along with such supportive information as a similarly projected graticule and/or land-area outlines — in order to produce a map. The coordinate points associated with isolines that were constructed on the sphere, however, must be projected — in the same way as any background information — prior to scaling and plotting.

A Comparison of Spherically- and Cartesian-Derived Annual Air Temperature Maps

In order to illustrate the degree and nature of the error which can be produced on small-scale climate maps by projecting the data points prior to interpolation to a regular lattice and contouring, annual average air temperature ($^{\circ}\text{C}$) in the Northern hemisphere was sampled and alternately mapped by the above-described spherically- and Cartesian-based interpolation and contouring procedures. Using the data set compiled by Willmott *et al.* (1981), 100 stations were randomly drawn from the subset of stations bounded by $-170^{\circ} \leq \lambda \leq -50^{\circ}$ and $2^{\circ} \leq \phi \leq 90^{\circ}$ which resulted in a markedly uneven distribution of station locations (Figures 3 and 4). Two map projections — Lambert's equal-area and Miller's — representing the class of cylindrical map projections, were used to examine projection-related dissimilarities that can occur

between 1) isotherms that were estimated on the surface of the sphere prior to projection and 2) isotherms that were determined in Cartesian two-space from a previously projected set of data points. Cylindrical projections were examined because they comprise the largest group of projections used to portray meso- and macroscale climate fields. Projection-related translations were performed by an experimental version of MAPRO (Kansas Geological Survey 1981) and the land-area outlines were taken from WORLDDATABANK I (Central Intelligence Agency 1972).

Interpolation began with the superposition of a 4' of latitude by 5' of longitude lattice over the area to be mapped. A grid size of 4' × 5' was chosen because it is frequently used in global climate models. Grid point estimates of air temperature and, subsequently, isotherm positions first were computed for the spherical distance and directional relationships between the data and grid points. The λ and ϕ coordinates associated with each spherically-estimated isotherm and map were then two-times projected into Cartesian two-space, i.e., by Lambert's equal-area and Miller's projections. Two comparable Cartesian-derived isotherm maps next were constructed by producing two projected sets of data points — using Lambert's and Miller's projections — from each of which Cartesian-based interpolations to a correspondingly projected (now rectangular) 4' × 5' grid then were made. The two Cartesian-estimated, grid point air temperature fields were each separately contoured within their respective projected Cartesian spaces. Once again, all computations were carried out by the modified versions of Shepard's (1968) function and the isoline lacing algorithms described in the preceding sections.

Before examining individual differences between spherically- and Cartesian-derived isotherm patterns, certain characteristics that the maps presented here have

in common — owing largely to assumptions embodied in Shepard's (1968, 1983) algorithm — should be mentioned (Figures 3 and 4). Where the station network is sparse, both the spherical and Cartesian versions of Shepard's function will extrapolate into the voids in such a way that the gradient of the temperature surface will diminish with distance from the nearest data points. This is why, for instance, the isotherms spread apart between Hawaii and Central America. In a few instances, where a large area contains but a single datum, the data point over-influences nearby and not-so-nearby grid points which in turn creates a flattening of the interpolated surface about the data point, e.g. around Hawaii. Near the edge of the flattening — as a consequence — the surface gradient must rapidly increase in order to account for the influence of "new" data points that have come within the search radii of the local grid points. The steep north-south gradient between Hawaii and Alaska at approximately 40° N latitude — evidenced by the convergence of the isotherms (Figures 3 and 4) — exemplifies this errant tendency.

No attempt has been made to smooth the isotherms — in order to circumvent an extra computational expense — and, therefore, they have a slightly jagged appearance. At the scale these maps are presented, however, the lattice is relatively fine and, therefore, the maps' appearance is not seriously compromised. The relatively fine texture of the grid further allows for a certain clarity of interpretation insofar as the error exhibited by the Cartesian-derived isolines can be ascribed to the interpolation process even though, generally speaking, isoline misplacements result from the compound of interpolation and contouring errors.

When the relationships between the data and grid points on the sphere are preserved during the contouring process, the relative positions of isotherms remain

constant regardless of the map projection (Figures 3 and 4). In cases where the data points are projected prior to Cartesian-based interpolation and contouring, however, the locations of isotherms relative to each other and to the supplemental map information (e.g., land-area outlines and data station locations) will inconsistently change from one irregularly spaced station distribution to another as well as from one projection to another. The inconsistency with which such errors are manifested from data set to data set and projection to projection is a result of synergism among the data point distribution, the pattern of the lattice and the inherent error associated with the map projection selected. That is, the error field on such a map may well be a unique result of the combined influences of the above three factors and, therefore, rather difficult to evaluate. When isotherms also have been estimated on the sphere, however, they may be compared to the Cartesian-derived isotherms for any particular map of interest.

Miller's cylindrical projection — in combination with the data and grid point distributions — produced the most striking differences between the spherically- and Cartesian-estimated isotherm locations (Figure 3). In the high latitudes — where the projection is highly exaggerated and there are few data points — there is a marked disparity between the two sets of isotherm patterns. When the corresponding spherically- and Cartesian-interpolated grid point values were subtracted from one another, the magnitudes of the differences in the higher latitudes ($\phi > 60^\circ$) were frequently in excess of 5° or 10° C. The Cartesian-derived isotherms generally fall north of their spherically-computed counterparts because the projection places the data points progressively further apart as the pole is approached. Another expression of the high-latitude error field is the Cartesian-derived -5° and -10° C isotherms

which head northwest from about 70° north latitude with the cooler of the two ultimately passing through the pole. Since it is well-known that annual isotherms ring the poles — as is evident among the spherically-derived isotherms — there is a very small possibility that the Cartesian-derived -5° and -10° C isotherms are correct. Such errors are common when Cartesian-based interpolations are made within a cylindrically-projected two-space although, in this instance, the errant tendency is somewhat intensified by Shepard's constraint on the extrapolated surface gradient. Where the data points are most dense (e.g., in the United States) the agreement between the two isotherm systems is the best — although discrepancies still are apparent.

On Lambert's cylindrical projection, where latitude is compressed as the pole is approached in order to preserve the equal area property, the errors are similar in magnitude to those associated with Miller's projection (Figure 4). In this instance, however, the data points are placed increasingly near one another as the pole is approached which, in turn, creates an unrealistically high local variance in air temperature at the higher latitudes. As the Cartesian-based interpolation and contouring procedure treats the pole as a line on such cylindrical projections, the abnormally high variance in temperature causes large fluctuations in the interpolated field and its isothermal representation. Most notably, this can erroneously cause multiple isotherms to pass through the pole. Once again, within the area where the distribution of data points is the most dense, the Cartesian- and spherically-derived isotherms agree, but not perfectly.

Symptoms such as these are typical of small-scale, Cartesian-based maps which employ cylindrical projections, especially when such a map surface includes the higher

latitudes. As mentioned above, when a cylindrically-projected map encompasses the full 360° range of longitude, it also is quite common for east-west trending isolines not to connect at the common longitude represented by the map's vertical edges. It should be emphasized, however, that such errors also exist on all small-scale, Cartesian-derived isoline maps although their identification often is difficult because 1) the map does not extend to at least one of the poles or over 360° of longitude, 2) the interpolation and/or contouring process may be constrained near the map borders in order to make the map appear correct, or 3) too little information about the interpolation and contouring methods is provided for the map-reader to make a meaningful evaluation. For these reasons, we recommend that interpolation to a regular latitude and contouring should take place on the surface of the sphere after which the isolines and other map information may be projected.

Summary and Conclusion

A sensitivity study of the errors which can occur on small-scale climate maps as a result of the common practice of projecting the data points prior to interpolation and contouring has been presented. Working from Shepard's (1968, 1983) well-known, local-search interpolation function, two algorithms that perform the interpolation and contouring process 1) on the surface of the sphere and 2) in Cartesian two-space are developed and described. In order to illustrate the nature and magnitude of the differences that can occur between spherically- and Cartesian-derived interpolations and contours, mean annual air temperature over the western half of the northern hemisphere — represented by 100 randomly selected stations — was alternately mapped by the two algorithms on two well-known map projections.

When the spherically-derived isotherm maps — assumed to be correct — were superimposed over the Cartesian-interpolated and contoured maps, the error fields manifested by the latter approach became apparent. With regard to our air temperature examples, local errors as large as 5° to 10° C commonly appeared in those regions that contained few data stations or had large projection distortion. When a Cartesian-derived, small-scale climate map encompasses most of the globe, however, two characteristic errors often can be observed without the benefit of a spherically-derived standard. On such maps, it is common to find more than one isoline passing through a pole or east-west trending isolines not to meet at the common longitude portrayed by the vertical edges of the map.

Our findings strongly suggest that the interpolation to grid points and subsequent contour lacing on small-scale climate maps should, in virtually all cases, be carried out on the surface of the sphere. To do otherwise is to assure that calculations performed on the interpolated grid point values or climatic inferences made from the isoline representations of the raw and gridded data fields will be in error. Since our spherically- and Cartesian-based version of Shepard's algorithm and their accompanying contour-lacing procedures are logically identical — save that one set computes spherical distances and directions and the other Cartesian — our findings further suggest that comparable errors will result from the use of any Cartesian-based interpolation and contouring method.

Acknowledgements

We wish to thank James E. Burt, Franklin E. Gossette, David R. Legates and Yale Mintz for their insights and technical assistance. The financial support of the Laboratory for Atmospheric Sciences at NASA's Goddard Space Flight Center (NASA grant NAG 5-107) also is gratefully acknowledged. Any errors that have gone undetected are entirely the responsibility of the authors.

References

- Akima, H. 1978. A method of bivariate interpolation and smooth surface fitting for irregularly distributed data points. *ACM Transactions on Mathematical Software* 4(2): 148-159.
- Barnes, S. L. 1964. A technique for maximizing details in numerical weather map analysis. *Journal of Applied Meteorology* 3: 396-409.
- Central Intelligence Agency 1972. *WORLDDATABANK I*.
- Cressman, G. P. 1959. An operational objective analysis system. *Monthly Weather Review* 87: 367-374.
- Fritsch, J. M. 1971. Objective analysis of a two-dimensional data field by the cubic spline technique. *Monthly Weather Review* 99: 379-386.
- Gandin, L. S. 1963. *Objective Analysis of Meteorological Fields*. Leningrad: Gidrometeorologicheskoe Izdatel'stvo. Translated from Russian by the Israel Program for Scientific Translation, Jerusalem, 1965, 242pp.
- Halem, M., Kalnay, E., Baker, W. E., and Atlas, R. 1982. An assessment of the FGGE satellite observing system during SOP-1. *Bulletin of the American Meteorological Society* 63: 407-426.
- Kansas Geological Survey 1981. *MAPRO*, (personal communication).
- (ed.), D. F. Marble 1981. *Computer Software for Spatial Data Handling*. Ottawa: International Geographical Union, Commission on Geographical Data Sensing and Processing.
- McCullagh, M. J. 1981. Creation of smooth contours over irregularly distributed data

using local surface patches. *Geographical Analysis* 13: 51-63.

Morrison, J. L. 1974. Observed statistical trends in various interpolation algorithms useful for first stage interpolation. *The Canadian Cartographer* 11: 142-159.

Panofsky, H. A. 1949. Objective weather-map analysis. *Journal of Meteorology* 6: 386-392.

Peucker, T. K. 1980. The impact of different mathematical approaches to contouring. *Cartographica* 17: 73-95.

Rhind, D. 1975. A skeletal overview of spatial interpolation techniques. *Computer Applications* 2: 293-309.

Rivin, G. S. and Kalikov, A. I. 1982. Mapping fields of the meteorological elements given at the nodes of a latitude-longitude grid. *Meteorologiya i Gidrologiya* (1): 41-48. the page range on the translation is 31-37.

Sampson, R. J. 1978. *SURFACE II Graphics System (Revision One)*. Lawrence, Kansas: Kansas Geological Survey.

Schlatter, T. W., Branstator, G. W., and Thiel, L. G. 1976. Testing a global multivariate statistical objective analysis scheme with observed data. *Monthly Weather Review* 104: 765-783.

Shepard, D. 1968. A two-dimensional interpolation function for irregularly-spaced data. *Proceedings—1968 ACM National Conference* : 517-524.

Shepard, D. 1983. Computer mapping: the SYMAP interpolation algorithm. In *Spatial Statistics and Models*, ed. G. L. Gaile and C. J. Willmott, Dordrecht, Holland: D. Reidel. — in press.

Wahba, G. 1979. *Spline Interpolation and Smoothing on the Sphere*. University of Wisconsin, Madison. Tech. Report No. 584.

Wahba, G. 1981. Spline interpolation and smoothing on the sphere. *SIAM Journal of Scientific and Statistical Computing* 2(1): 5-16.

Wahba, G. and Wendelberger, J. 1980. Some new mathematical methods for variational objective analysis using splines and cross validation. *Monthly Weather Review* 108: 1122-1143.

Willmott, C. J., Mather, J. R., and Rowe, C. M. 1981. Average Monthly and Annual Surface Air Temperature and Precipitation Data for the World: Part 2. The Western Hemisphere. *Publications in Climatology* 34(2)

Figure Captions

Figure 1. Schematic representations of an irregularly distributed set of data points (\circ 's) and of grid nodes (\square 's) a) on the sphere and b) projected into Cartesian two-space. Also illustrated are the corresponding distance ($d_{j,k}^s$ and $d_{j,k}^c$) and directional ($\theta_j^s(k,l)$ and $\theta_j^c(k,l)$) relationships between the data and grid points in spherical (superscript s) and Cartesian (superscript c) space. It should be noted that $\theta_j^s(k,l) \neq \theta_j^c(k,l)$ or $d_{j,k}^s \neq d_{j,k}^c$ or both.

Figure 2. Schematic diagrams depicting the placement of a) spherical and b) Cartesian grid cell centers (Δ 's) and the subdivision of each grid cell into four triangular sub-cells. A hypothetical isoline (dashed) has been laced through the triangular mesh -- intersecting the edges of triangular sub-cells at points (\circ 's) determined by either great circle or linear interpolation between the end-point values of the intersected edges -- in order to illustrate the contour placement procedure.

Figure 3. Isothermal representations of mean annual shelter-height air temperature ($^{\circ}\text{C}$) over the western half of the northern hemisphere using Miller's cylindrical projection. From 100 irregularly spaced data points (Δ 's), temperatures were interpolated to a regular $4' \times 5'$ lattice and subsequently contoured. The solid isotherms represent the interpolation and contouring process as performed on the surface of the sphere *prior* to Miller's projection whereas the dashed isotherms depict the interpolation and contouring process as carried out in Cartesian two-space *following* Miller's projection of the data points into two-space.

Figure 4. Isothermal representations of mean annual shelter-height air temperature ($^{\circ}\text{C}$) over the western half of the northern hemisphere using Lambert's cylindrical equal-area projection. From 100 irregularly spaced data points (Δ 's), temperatures were interpolated to a regular $4' \times 5'$ lattice and subsequently contoured. The solid isotherms represent the interpolation and contouring process as performed on the surface of the sphere *prior* to Lambert's projection whereas the dashed isotherms depict the interpolation and contouring process as carried out in Cartesian two-space *following* Lambert's projection of the data points into two-space.

Figure 1

a. *Spherical Surface* b. *Cartesian Surface*

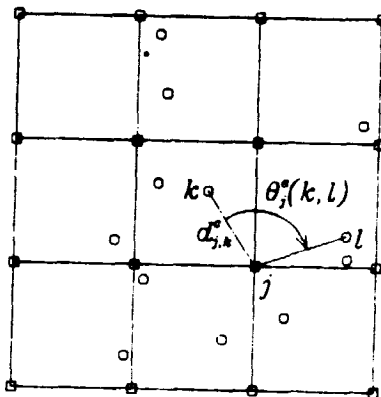
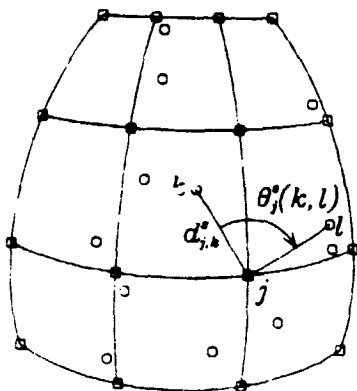


Figure 2

a. *Spherical Surface* b. *Cartesian Surface*

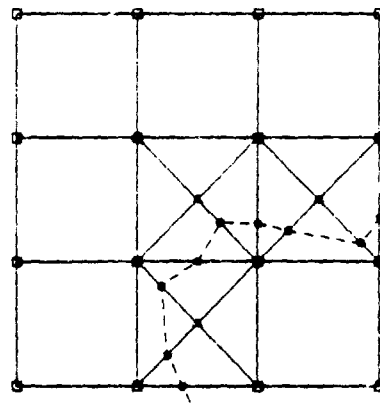
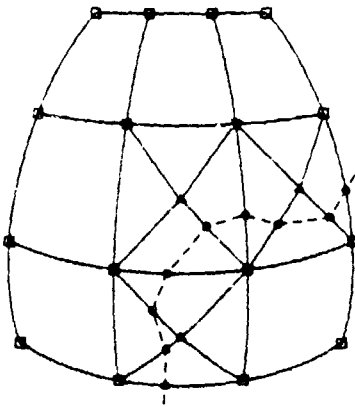
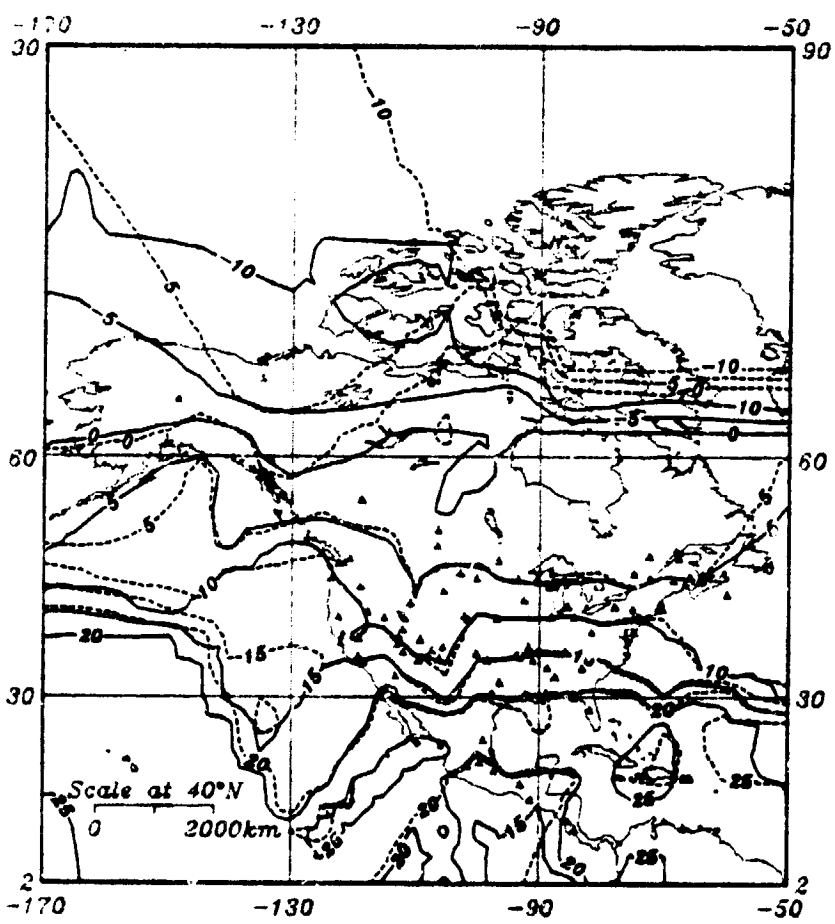
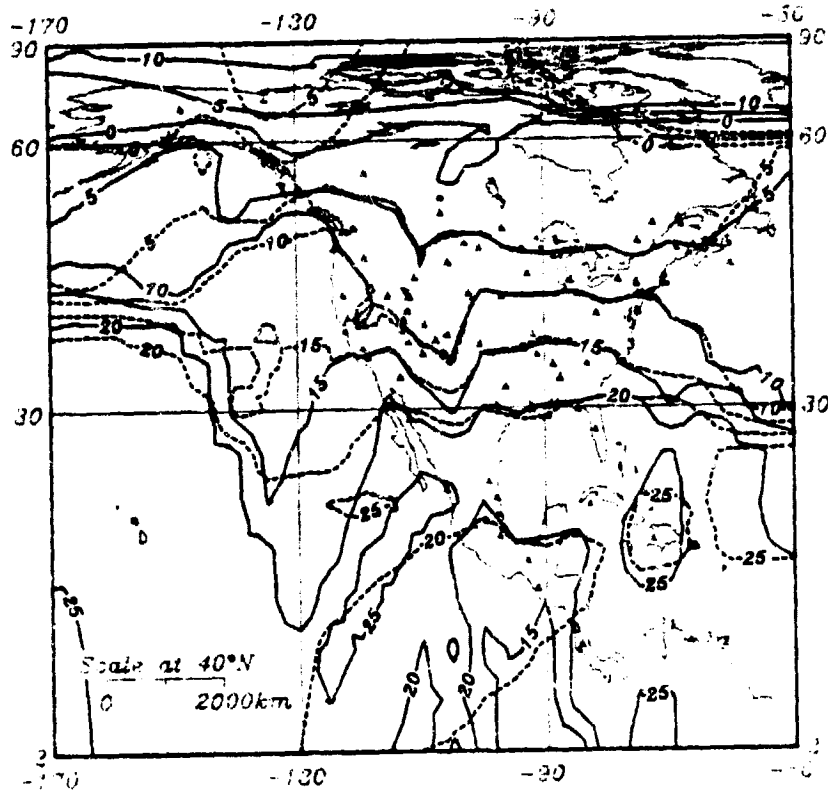


Figure 3



ORIGINAL PAGE IS
OF POOR QUALITY

Figure 4



APPENDIX 2

An Empirically-derived Climatology of the
Terrestrial Seasonal Water Cycle.

An Empirically-Derived
Climatology of the Terrestrial
Seasonal Water Cycle

by

Cort J. Willmott
Clinton M. Rowe

Center for Climatic Research
Department of Geography
University of Delaware
Newark, Delaware 19716

and

Yule Mintz

Department of Meteorology
University of Maryland
College Park, Maryland 20742

also

Laboratory for Atmospheric Sciences
NASA Goddard Space Flight Center
Greenbelt, Maryland 20771

with
3 figures

February 1984

2/7/84
Gave a copy
to Yale to
proof.

Draft

ABSTRACT

A zeroth-order approximation of the large-scale spatial and seasonal variability associated with terrestrial snow cover, soil moisture and evapotranspiration is presented and evaluated. These surface climate fields were obtained through (1) an empirically-based water budget analysis of 13,332 station records which contained average monthly air temperature and precipitation observations (Willmott ~~et al.~~, 1981) and (2) the spatial interpolation of the estimates to regular, general circulation model-compatible lattices (1° of latitude by 1° of longitude and 4° by 5°). The grid-point seasonal cycles associated with the $4^\circ \times 5^\circ$ mesh then were harmonically decomposed and the first two harmonics evaluated. Seasonal snow cover exhibited the most coherent space-time distributions whereas the soil moisture cycle was the most variable. Evapotranspiration displayed moderate levels of space-time variability.

INTRODUCTION

Sensitivity experiments with atmospheric general circulation models (GCMs) repeatedly have demonstrated the profound influence which the near-surface, terrestrial water balance exerts on climate (Mintz, 1982). Available soil moisture and surface water (e.g., snow cover) are principal agents in the determination of regional albedo and, perhaps more importantly, they largely control the partitioning of the surface enthalpy flux between latent and sensible heat. The degree to which surface enthalpy flux is comprised of latent or sensible heat has climatic significance for the following reasons: sensible heat transfer from the terrestrial surface warms the local boundary layer whereas latent heat is usually realized in the free atmosphere during the condensation process--frequently at considerable distance from where it is added to the boundary layer. Ensuing dissimilarities in the vertical, spatial and temporal distributions of these two sources of atmospheric heat make the general circulation of the atmosphere (i.e., the thermally induced large-scale motion) sensitive to the near-surface convective fluxes. The moisture associated with latent heat flux from the land surfaces⁻⁻⁻evapotranspiration--is additionally important because it represents the major source of moisture for terrestrial precipitation (Mintz, 1982).

Since most GCMs use a one- or two "bucket" representation of the near-surface water balance (Carson, 1981) and it has been demonstrated that this over-simplification is prone to error (Mintz et al., 1983; Sellers, 1981), improvements in GCM-representations of the near-surface water balance are prerequisite to a fuller understanding of atmospheric circulation and climate. More realistic analogs of the role that the terrestrial biosphere plays in the water balance promise to remove much of the uncertainty and inaccuracy associated with the open-bucket approach (Dickinson, 1983; Mintz et al., 1983).

Another problem has been and continues to be the paucity of reliable, observed global water balance data which are available for the operational and scientific evaluation of GCM predictions of the seasonal water cycle as well as for use as sub-annual initial or boundary conditions by GCMs. Jaeger's (1983) discussion of global precipitation data sets well illustrates this problem. Observed climate fields have additional utility in that inductive evaluations may reveal patterns and provide insights which may lead to improved GCM-representations of the climate system. Sub-annual precipitation and air temperature fields (seasonal and monthly) have been observed and compiled (e.g., Möller, 1951; Jaeger, 1976; Steinhauser, 1979; Willmott et al., 1981) but large-scale, sub-annual fields of evapotranspiration, soil moisture and snow cover are not well-represented in the literature. Baumgartner (1981), for instance--in his review of the large-scale water balance literature--noted that "World wide water balances for shorter periods than a year are not available at the moment." Efforts to upgrade both GCM-characterizations of the near-surface water budget (e.g., Mintz et al., 1983) and the store of empirically-derived sub-annual water budget observations (e.g., Willmott et al., 1981) are ongoing by the authors although this paper is restricted to the presentation of heretofore unavailable monthly water budget data and inferences that can be drawn from those data.

Mid-monthly values of terrestrial soil moisture, snowpack water equivalent and evapotranspiration were derived from a global air temperature and precipitation data set (Willmott et al., 1981) by means of an empirically-based water budget algorithm. Since the water budget method employed represents a substantial revision of a previously published procedure (Willmott, 1977), it will be described in the next section of the paper with an emphasis on pertinent upgrades. Our estimates of the seasonal soil moisture, snow cover and evapotranspiration cycles as they vary across the world's land surfaces are presented

and evaluated in third section of this paper and concluding remarks follow.

CLIMATIC WATER BUDGET

A simple water balance algorithm, which could be used with monthly air temperature and precipitation observations taken from any terrestrial location, was developed from a similar, existing model (Willmott, 1977). The procedure assumes that monthly evapotranspiration (E_m) can be adequately evaluated by a calculation of the form

$$E_m = \beta_m E_m^0 \quad \text{mm month}^{-1}$$

where β_m represents the integrated conductance of the biosphere (near-surface plant-soil-water-atmosphere system) to evapotranspiration and E_m^0 is reference crop or potential evapotranspiration. Computations are made daily and summed in order to obtain monthly totals.

Unadjusted reference crop evapotranspiration is first estimated according to Thornthwaite's (1948) method; that is,

$$E_m^0 = \begin{cases} 16 (10 \bar{T}_m / I)^a, & 0 \leq \bar{T}_m < 26.5 \\ -415.85 + 32.24 \bar{T}_m - 0.43 \bar{T}_m^2, & \bar{T}_m \geq 26.5 \end{cases} \quad \text{mm month}^{-1}$$

where E_m^0 is set equal to zero when ($\bar{T}_m < 0$), \bar{T}_m is the average shelter height air temperature ($^{\circ}\text{C}$) for month m , I is the station heat index and a is an empirically-derived constant. The latter two terms are obtained from

$$I = 12N^{-1} \sum_{m=1}^N (\bar{T}_m / 5)^{1.514}$$

and

$$a = 6.75 \times 10^{-7} I^3 - 7.71 \times 10^{-5} I^2 + 1.79 \times 10^{-2} I + 0.49$$

where N is the number of months or days from which a representative station heat index may be calculated. It (N) is usually a multiple of 12 or 365 for monthly or daily budgets, respectively. After E_m^0 has been computed, it is adjusted for variable day and month length according to

$$E_m^0 = E_m^0' [(\theta_m/30)(\theta_d/12)] \quad \text{mm month}^{-1}$$

where θ_m is the length of month m (days) and θ_d is the length of day (hours).

Thorntwaite's (1948) estimate of regional E_m^0 occasionally has been criticized because it is not biophysically-based (e.g., Lee, 1978) and it is thought to yield insufficiently accurate values of E_m^0 (Jensen, 1973). Such evaluations seem quite reasonable upon cursory examination but more careful investigation suggests that a number of the commonly-leveled criticisms may be over-stated. It should also be kept in mind that Thorntwaite's estimates only require average air temperature data which are widely available and which represent fewer input requirements than most competitive methodologies (e.g., see Jensen, 1973).

By making E_m^0 an empirical function of \bar{T}_m , Thorntwaite (1948) was not ignoring the salient biophysics of which he was well-aware (Thorntwaite and Holzman, 1939) but rather he was attempting to make use of a weather variable that represented the integration of all the flux terms pertinent to the estimation of regional E_m^0 . Too often, it is forgotten that E_m^0 responds to warm and cool air advection as well as to irradiance and that the combined, temporally-integrated influences of these two fluxes on E_m^0 covaries with the vicissitudes in \bar{T}_m . In other words, while the form of Thorntwaite's model can only be partially justified on biophysical grounds and the magnitudes of his coefficients have virtually no biophysical interpretation, his selection of \bar{T}_m as the independent variable, as opposed to net irradiance for instance, is well-taken on both biophysical and practical grounds. In the end, however--Thorntwaite's

biophysical insights notwithstanding--it primarily is a mathematically-based model (Willmott, 1984a) which was pragmatically developed for predictive, not explanatory, purposes. As a consequence, the main criteria on which this formulation should be evaluated include: economy, ease of use and, most importantly, accuracy.

Thornthwaite's model is often thought to produce inaccurate estimates of E_m^0 --relative to many of the competing procedures--and this conclusion is based largely upon comparisons with lysimeter observations. Jensen (1973), for example, compared 18 frequently used methods of estimating E_m^0 with monthly lysimeter observations drawn from ten sites and he concluded that Thornthwaite's model "did not produce estimates that agreed well with measured values," i.e., the estimates were virtually all low. On the average, the root mean square error (RMSE) was 1.84 mm day^{-1} . If the measured values are correct, this error would be unquestionably large; however, since lysimeters often overestimate regional E_m^0 , it is likely that Thornthwaite's values are closer to actual, regional E_m^0 than commonly believed. In fact, if one assumes that the systematic difference between Thornthwaite's E_m^0 and the lysimeter estimates of E_m^0 can be attributed to the lysimeter-derived values, the RMSE expectation reduces to 0.92 mm day^{-1} (Willmott, 1984b) which is quite competitive (Jensen, 1973). For the sake of brevity, the above discussion somewhat oversimplifies an ongoing evaluation of Thornthwaite's method; nevertheless, these and other findings suggest that the Thornthwaite model provides more accurate estimates of regional E_m^0 than is generally believed.

In addition to the Thornthwaite estimate of E_m^0 , the water budget calculations require monthly precipitation information which is assumed to be in liquid form (P_m^r) when ($\bar{T}_m \geq -1$); otherwise, precipitation is treated as snowfall

(P^s_m). Estimates of E^O_m , P^r_m and P^s_m remain constant over the course of month m whereas the storage terms (i.e., soil moisture ^{and snowpack} / ~~snow~~ water equivalent) and actual evapotranspiration are computed daily in order to partially account for the nonlinear, time-dependent relationships between E^O_m , P^r_m , P^s_m and actual monthly evapotranspiration-- E_m .

Terrestrial water storage is partitioned between a snow cover and a soil moisture store where the latter has a saturation or field capacity (w_*) which must be specified prior to calculation. In this instance, w_* was held constant at 150 mm which is large for ^{many} ~~most~~ soils that underlie grasses and other low vegetation, and small for most forest-covered soils. Sensitivity comparisons between $w_* = 150$ and more representative biome-specific values suggest ^{that} $w_* = 150$ yields an acceptable error response in nearly all biomes. Since E^O_m , P^r_m and P^s_m are taken to be constant over month m and the water budget is evaluated on approximately a daily basis (i.e., 30 times per month), the daily estimates of reference crop evapotranspiration, rain- and snowfall are $E^O_{md} = E^O_m/30$, $P^r_{md} = P^r_m/30$ and $P^s_{md} = P^s_m/30$ where d refers to the day of hypothetical 30-day month m .

Quasi-daily evaluation of the snow and soil moisture stores begins with the estimation of the water contained in the snowpack. At the end of day d , the water content of the snowpack is

$$w^s_{md} = w^s_{md-1} + P^s_{md} - M_{md} \quad \text{mm}$$

where w^s_{md-1} is the water equivalent of the snowpack at the end of the previous (d-1) day and M_{md} is the snowmelt during day d . Daily snowmelt is estimated from

$$M_{md} = 2.63 + 2.55 \bar{T}_{md} + 0.0912 \bar{T}_{md} P^r_{md} \quad \text{mm day}^{-1}$$

where M_{md} is constrained so that it cannot be less than zero or greater than $(w_{md-1}^s + P_{md}^s)$. Comparisons between the above equation and the data from which it was derived--representing three dissimilar drainage basins and 113 observations (Anderson, 1973; Pysklywec et al., 1968; Storr, 1978)--suggest a moderately good fit, i.e., RMSE = 6.62 mm day⁻¹ and $r^2 = 0.59$. Evaporative demand from the surface or soil water surplus (D_{md}) subsequently is calculated as

$$D_{md} = M_{md} + P_{md}^r - E_{md}^o \quad \text{mm day}^{-1}$$

When D_{md} is negative, it represents a demand and it constitutes a surplus when it is positive. The degree to which the biosphere facilitates evapotranspiration can be estimated according to

$$\beta_{md} = \begin{cases} 1 - \exp(-6.68 w_{md-1}/w_*) & , D_{md} < 0 \\ 1 & , D_{md} \geq 0 \end{cases}$$

where w_{md-1} is the soil moisture at the beginning of day d . Using data from Davies and Allen (1973), the constant (6.68) was translated from a best fit described by Nappo (1975). Available soil moisture at the conclusion of day d then becomes

$$w_{md} = w_{md-1} + \beta_{md} D_{md} \quad \text{mm} \quad \leftarrow$$

If w_{md} exceeds w_* , the difference is retained as a surplus (s_{md}) for day d and w_{md} is set equal to w_* . The increase or decrease soil moisture during month m then can be defined as

$$\Delta w_m = w_{m30} - w_{m-1, 30} \quad \text{mm}$$

When the temperature and precipitation timeseries (vectors) are continuous, span one or more complete years and each element of those vectors is a climatic normal or representative average; a water balance may be assumed.

In such cases, an iterative solution to the above-described set of equations is possible where the iteration continues until the quasi-daily soil moisture and snow cover vectors (\underline{w} and \underline{w}^s respectively) become virtually invariant. Note that each of these vectors has $30N_m$ elements where N_m is the number of months over which the water balance is computed. Actual monthly evapotranspiration then may be obtained from

$$E_m = p_m^r + \sum_{d=1}^{30} M_{md} - \Delta w_m - \sum_{d=1}^{30} s_{md} \quad \text{mm month}^{-1}$$

and the monthly soil moisture deficit is $\delta_m = E_m^0 - E_m$. Representative monthly soil moisture and snow cover values then are taken as those elements of \underline{w} and \underline{w}^s that correspond to the fifteenth of each month evaluated.

TERRESTRIAL SEASONAL WATER CYCLE

Using the procedure described in the above section, annual water balances were computed for 13,332 stations from average monthly air temperature and precipitation data (Willmott et al., 1981). At each station, the water balance was iteratively solved and the solution sets of monthly total evapotranspiration (E_m), mid-monthly soil moisture (w_m) and mid-monthly water equivalent of the snowpack (w_m^s) are evaluated. ←

Following their estimation, each irregularly-spaced climate field, e.g., the January evapotranspiration estimates (E_1) associated with the 13,332 station locations, was used to spatially interpolate additional values at the nodes of a 1° of latitude by 1° of longitude lattice. The interpolations were performed by a method described by Willmott et al. (1984) with the exception that the number of "nearby" data points (stations) which influenced a grid point value was held constant at 10. This modification of Willmott et al. (1984) has the effect of dampening the spatial variance among grid points when ←

stations are sparsely located and accentuating the local variability when stations are in close proximity to one another. In order to preserve map clarity, we report on a subset of the interpolated water budget fields that is associated with the nodes of a 4° of latitude by 5° of longitude grid--which is frequently used in GCM applications.

Snow Water Equivalent

Statistics that summarize the water balance-predicted seasonal progression of snow cover (in a water equivalent depth of mm) are generally consistent with climatological expectation and with available observations (e.g., Dewey and Heim, 1981), although no truly comparable data set exists to the authors' knowledge. The average quantity of water entrained in the snowpack (\bar{w}^s) increases with the magnitude of latitude, particularly in the Northern Hemisphere, although certain mesoscale departures are apparent (Figure 1a). Greater average snow depths, for example, occur within the continental climates of eastern North America owing to the synergy between relatively high precipitation rates in winter and the ^{low} temperatures that persist in the absence of a marine influence. The accentuating impact of orography and the lower air temperatures of the mid-latitude mountain ranges are evident, for instance, in the Rocky and Ural mountains. Owing to the general poleward decrease in land area and elevation in the Southern Hemisphere, this region--by contrast ^{low} has few locations with a seasonal snow cycle (Koliakov and Krenke, 1981) or an average snow water equivalent of more than 10 mm (Figure 1a). Antarctica, of course, is the exception and the water balance estimates a variable but perennial snow-ice cover which, at virtually all locales, is well in excess of 500 mm.

Expressed as the standard deviation associated with the seasonal snow cover cycle ($\hat{\sigma}^s$), the spatial distribution of temporal variability also is consistent with climatological expectation (Figure 1b). Where the snow cover

is seasonal (i.e., it completely melts in the summer), $\hat{\sigma}^S$ is colinear with \bar{w}^S since w_m^S is bounded on the low end by zero. Moving northward, along the east coast of North America for example, the seasonal variance increases with latitude to approximately 50°N where $\hat{\sigma}^S$ begins to lessen because of the decline in winter precipitation and the reduction of the melt season length. Mountainous regions exhibit large seasonal variances as well as large average snow covers (Figure 1b). Antarctica has relatively small variances that, once again, decrease with increases in the magnitude of latitude.

Although the spatial distributions of the first and second moments associated with the seasonal snow cover cycle (Figure 1a and 1b) well-describe average snow cover and the degree to which snow cover varies seasonally, they do not provide information about the temporal progression of the seasonal cycle; for instance, the times of the year when extrema occur and the amplitudes associated with the main periodicities. These aspects of the seasonal cycle, however, can be described by means of the harmonic decomposition of the monthly timeseries. A location's seasonal snow cover cycle may be represented by

$$w_m^S = \bar{w}^S + \sum_{k=1}^6 w_k^S \cos[\pi(km - m'_k)/6] \quad \text{mm}$$

where w_k^S is the amplitude of the k-th harmonic, k is the frequency and m'_k is the phase angle in months. The parameters w_k^S and m'_k (k = 1, 6) then provide a complete description of the seasonal cycle. Since the higher-frequency harmonics typically explain local or trivial portions of $\hat{\sigma}^S$ their interpretation is often of limited value. For this reason, we present only the parameters associated with the first two harmonics which, at the mesoscale, introduce an acceptable error-level. Over the continents of both the Northern

and Southern Hemispheres, the magnitude of the variance left unexplained by the first two harmonics $[(1 - r^2)\hat{\sigma}^s]^2$ usually is not much greater than 10 mm (Figure 1c).

Phase angles associated with the first harmonic ($k = 1$) clearly represent the end of the accumulation season (winter) and the onset of melt (Figure 1d). A clockwise shift in m'_k from January and February, near the snowline, to March and April in the higher latitudes is evident in both North America and Northern Asia. Regions such as eastern North America, that are little-influenced by maritime air in the winter, also exhibit an extended accumulation season. Local increases in both the water equivalent of the snowpack and the length of the accumulation season additionally appear in mountainous areas (e.g., the Sierra Nevada, the Pyrenees and the Himalayas). Consistent with the spatial distribution of $\hat{\sigma}^s$, the amplitudes associated with the first harmonic are greatest in the latitude band where winter, frontal snow most frequently falls. Similar patterns also appear in Antarctica but, of course, they are four or five months out of phase (Figure 1d).

Phase shifts (m'_k/k) associated with the second snow cover harmonic (Figure 1e) are approximately equivalent to the phase angles of the first harmonic--near the equatorward limits of the seasonal snowpack. Angular departures of $m'_2/2$ from m'_1 , however, increase with the magnitude of latitude. The rotation of these departures is clockwise in the Northern Hemisphere and counterclockwise in the Southern Hemisphere. Second harmonic amplitudes also covary positively with the magnitude of latitude. In the lower latitudes where $m'_1 \approx m'_2/2$, the "direction" of $m'_2/2$, relative to m'_1 , indicates that the temporal range of the snow cover is confined to a relatively short snow accumulation season. As the magnitude of latitude increases, however, $m'_2/2$

rotates in a clockwise procession from m'_1 in order to account for the lengthening of the snow accumulation season. A concomitant increase in the snow water equivalent (represented by the amplitude) confirms the increasing importance of this extension in the length of the snow cover season with latitude. Although most of the spatial variance in $(m'_2/2 - m'_1)$ can be explained by latitude alone, the melt process is regulated by the available energy and, therefore, the patterns are synoptically modified in some cases. Note the shortening of the snow cover season in northern Scandinavia relative to areas at the same latitude in eastern Siberia due to maritime warming.

Soil Moisture

Estimated mean soil moisture is much more spatially variable than average snow cover owing to its dependency on and interaction with a greater number of "independent" variables such as field capacity, biospheric conductance (β_m) and reference crop evapotranspiration (Figure 2a). Certain large scale patterns, however, are apparent and are consistent with well-accepted climatic principles. The humid eastern portion of North America, for example, has plentiful soil moisture throughout most of the year as manifested by averages well-above 125 mm--assuming a field capacity of 150 mm. By contrast, the drier reaches of the western plains states as well as of the Sierra Nevada average \approx 25 mm. Orography along the northwest coast provides a thin ribbon of land with seasonally high precipitation (winter maximum) which is manifested in much higher soil moisture averages than the nearby mountain and valley regions that lie to the east.

South America too exhibits familiar patterns (Figure 2a). A very dry west coast ($\bar{d} \leq 25$ mm) extends from northern Peru (near the equator) to central Chile and then southeast into Patagonia which lies in the rainshadow of the southern Andes mountains. The windward side of the southern Andes and the

coastal zone, on the other hand, are quite moist. In eastern Brazil, the tropical rainforest exhibits similarly high average soil moistures owing to excesses of precipitation but these extend over a much greater area. High average soil moistures along the northeast coastal reaches of South America and as well as in southeastern Brazil also are correlated with high rainfall.

Within Europe, average annual soil moisture is spatially variable although, at the regional scale, few areas can be classed as dry (Figure 2a). Most of Europe exhibits plentiful precipitation which continually replenishes the soil moisture. Where eastern Europe grades into western and central Asia (i.e., beginning with the Caspian desert and the Ural mountains), precipitation is drastically reduced and the accompanying decreases in annual soil moisture are apparent over much of north-central Asia. Along the seasonally humid east coast of Asia, however, generally high--but locally variable--levels of precipitation provide relatively high levels of soil moisture (>125 mm) in Japan, Korea and areas north. South and Southeast Asia receive even higher rates of precipitation and, therefore, their soils are usually near saturation. Much of this rainfall is convectional (e.g., in Sumatra, Java and Borneo) although in Monsoon Asia (e.g., in Burma, Bangladesh and Vietnam) plentiful precipitation is dynamically (i.e., monsoonally and orographically) reduced during the summer.

Annual soil moisture patterns in Africa also spatially covary with precipitation (Figure 2a). Most striking, of course, is the Sahara Desert and circur-Sahara regions which together span northern Africa excepting the Atlas mountains and coastal areas of Morocco and northern Algeria. South of the Sahara, over much of central Africa as well as the Ivory Coast, the soil remains moist throughout the year (>75 mm) principally owing to convective

rainfall. Southwestern Africa, e.g., the Kalahari desert, by contrast is quite dry throughout the year.

Australia is very dry ($\bar{w} < 25$) over most of its interior (Figure 2a). The northern, eastern and southern coastal regions represent virtually the only moist regions on the continent.

Soil moisture variance associated with the seasonal cycle--as represented by the standard deviation (Figure 2b)--spatially covaries with the annual mean as well as with climatological expectation. The greatest seasonal variance occurs in subtropical regions that experience a marked seasonality in precipitation. Central America, Brazil and Africa, for instance, exhibit seasonal standard deviations greater than 50 mm. This also is true of Monsoon Asia. The substantial seasonality associated with Mediterranean climates (summer dry) also is manifested in large standard deviations of soil moisture along the northern coasts of the Mediterranean Sea and the western coast of North America. Local and mesoscale anomalies are common, indirectly owing to topographic and vegetation influences; nonetheless, soil moisture variance tends to be inversely correlated with the magnitude of latitude.

When the soil moisture variance is harmonically decomposed and the harmonics are interpreted, the seasonal soil moisture cycle can be understood more clearly. Two harmonics were sufficient to explain the majority of the variance contained in the seasonal soil moisture cycle (Figure 2c). The variation left unexplained by the two harmonics (error) is generally between 5 and 15 mm and only at a very few locations does it exceed 20 mm.

Most of the seasonal variation is explained by the first harmonic whose amplitudes frequently approach 100 mm although they (the amplitudes) are highly variable in space (Figure 2d). Phase angles associated with the first harmonic also are quite variable; once again, owing to the large influence that the

local environment exerts on soil moisture. In the mid- to high latitudes of the Northern hemisphere, the clockwise rotation of phase angles with latitude is partially due to the delay in the snowmelt process which results from reduced levels of available energy. That is, since the maximum levels of soil moisture often are associated with the infiltration of melt water, the seasonal soil moisture peak occurs shortly after the onset of melt. Over much of central North America and Asia, this occurs in March or April whereas it occurs in May or June in the north of Canada and Siberia. Inland and mountainous environs enhance this clockwise rotation, relative to other areas at the same latitude, and the effect is evident in the northern Rocky Mountains and Great Plains. The contribution of snowmelt to soil moisture in the higher latitudes is enhanced by the low magnitudes of potential evapotranspiration early in the growing season.

Equatorward of the seasonal snow line, snowmelt does not influence the timing of the soil moisture maxima. Rather, maxima commonly occur at the end of extended periods where precipitation exceeds evapotranspiration. Areas along the northern shore of the Mediterranean Sea, for instance, experience soil moisture maxima in late February and early March, i.e., at the end of the rainy season (winter), when potential evapotranspiration is still quite small. Deserts such as the Sahara and Gobi exhibit greatly reduced the amplitudes associated with the seasonal cycle as they are dry virtually the entire year. Subtropical climes, e.g., sub-Saharanⁿ Africa, Venezuela, and parts of South^s and Southeast Asia, have early-autumn maxima that occur in September or October. In many subtropical areas, the seasonal soil moisture cycle has a double maximum although the September-October peak is usually dominant. Early-autumn maxima result from the northward shift in the ITCZ and accentuated thermal convection which responds to the summer accumulation of net irradiance.

South of the equator, in subtropical South America, Africa, Borneo and so on, soil moisture maxima again coincide with precipitation maxima (Figure 2d); that is, they generally occur in February or March. These maxima are nearly six months out of phase with their Northern Hemisphere counterparts, and they also result from a shift in the ITCZ and thermally induced convection. Further south, the mid-latitude deserts, e.g., the Atacama, Kalahari and central Australian deserts, are perennially dry and, therefore, have no real seasonality. Maxima in southern Chile and Argentina as well as in ^South Africa and Australia occur in August and September (i.e., toward the end of winter) for the same reasons that they appear in February and March within similar locales in the Northern Hemisphere. In Antarctica, since the soil rarely thaws, no seasonal soil moisture cycle is apparent. ←

Within most of the seasonally snow covered reaches of the Northern Hemisphere, the vector field representing the second soil moisture harmonic is quite similar in appearance to the corresponding first harmonic field (Figure 2c). This suggests that snowmelt-induced maxima are especially well-defined. Over eastern North America and northwestern Asia, however, the phase shifts of the second harmonic are rotated clockwise with respect to the phase angles of the first harmonic in order to account for extended moist periods. In many instances, this pattern represents a secondary soil moisture maximum caused by summer precipitation which exceeds the environment's ability to evapotranspire the moisture. ←

Subtropical regions, e.g., in Mexico and sub-Saharan Africa, exhibit second harmonic phase shifts which are nearly six months out of phase with the first harmonic phase angles. This also means that the second peak ($m'_2/2 + 6$) associated with the second harmonic is in phase with the first harmonic. Such

patterns are a response to the marked precipitation seasonality of these regions, i.e., where most of the year is very dry and late summer is quite wet near field capacity (Willmott et al., 1981). South of the equator, the subtropical regions of Africa as well as much of central South America exhibit maxima in May or June which dampen the sub-zero lows in soil moisture predicted by the first harmonic in winter (e.g., June, July and August) and lengthen the wet-season which extends throughout the remainder of the year. Further south, the Southern Hemisphere deserts, e.g., the Atacama, Kalahari and Great Desert of Australia, have a virtually double seasonal cycle; that is, of frequency two. Eastern Australia and portions of southern central Africa, however, have maxima about February or March for similar reasons.

In Mozambique, for instance, the first ^{second harmonic} maximum occurs at the same time of year as the phase angle associated with the first harmonic in order to describe an accentuated seasonal maximum and dampen the seasonal minimum represented by the first harmonic. In eastern Australia, the second harmonic serves essentially the same purpose, except that the first harmonic is six months out of phase with its Mozambique counterpart.

Evapotranspiration

Except in regions that are seasonally water limited for one or more of a variety of reasons, mean evapotranspiration follows potential evapotranspiration which covaries with mean air temperature. For this reason, there is a general decrease in E_m with the magnitude of latitude (Figure 3a). Superimposed on this large-scale pattern are a number of mesoscale features.

In the Pacific southwest, southwest South America, central Asia, north Africa, southwest Africa and west-central Australia, low precipitation rates are responsible for relatively dry soils. This, in turn, provides that nearly

all the available energy is disposed of sensibly and that evapotranspiration is less than 25 mm/month over most of these zones. Similar average evapotranspiration rates occur in the high latitudes but for different reasons; that is, cold- climate evapotranspiration is limited by low E_m^0 levels. In stark contrast, the wet and seasonally-wet tropics and subtropics exhibit very high rates of evapotranspiration. Areas in Brazil, sub-Saharan Africa and southeast Asia, for example, evapotranspire well in excess of 100 mm/month. Thermally induced precipitation is seasonally or annually plentiful in these regions and available energy is relatively high over the entire year. Regionally characteristic, annual evapotranspiration rates also are apparent, in the seasonally humid east and southern United States. On the whole, because of their greater dependence on available energy (E_m^0), actual annual evapotranspiration fields tend to be smoother than corresponding soil moisture fields.

Standard deviations associated with the seasonal evapotranspiration cycles rarely exceed 50 mm/month although they are quite variable from region to region (Figure 3b). The more pronounced the seasonal temperature and/or precipitation cycle the greater the seasonal variance in evapotranspiration. When the air temperature falls to near or below freezing during the winter and then rises to over 20°C in the summer months and summer precipitation is plentiful, a large seasonal variance in evapotranspiration results. Mid-latitude regions such as the mid-western and eastern United States, and eastern Asia consequently have evapotranspiration standard deviations well over 50 mm/month. Monsoon Asia as well as sub-Saharan Africa similarly exhibit standard deviations greater than 50 mm/month. In the first case, this results from coincidence of very high levels of E_m^0 and dynamically induced summer precipitation. The

concurrence of high summer E_m^0 and precipitation also occurs in sub-saharan Africa; however, this precipitation is caused thermally rather than dynamically. Zones of low variance, on the other hand, occur in areas that have little seasonal variance in either precipitation or available energy. The rainforest of eastern Brazil, for instance, is warm and moist throughout the year whereas the Sahara and Gobi deserts as well as Antarctica are dry over the entire year. These regions vary by less than 10 mm/month. Moderately variable evapotranspiration cycles characterize much of the rest of the terrestrial world.

Most of the seasonal variability can be described by the first two harmonics associated with the evapotranspiration cycle as suggested by the map of unexplained variation (Figure 3c). Patterns in the seasonal evapotranspiration cycle as expressed by the first harmonic are coherent and can be explained by ^{accepted} ~~well-known~~ climate principles (Figure 3d). In the mid- and high-latitudes, most of the seasonal variance in E_m is explained by the first harmonic since E_m^0 follows the sun and, therefore, is inversely proportional to the magnitude of the latitude. It follows that the mid- and high-latitude evapotranspiration maxima should occur during the high-sun season--which they do. On the more humid, eastern portions of the continents, a lag (approximately one month) in the evapotranspiration maxima--behind the solar maximum--corresponds to the familiar peak in air temperature which also occurs after the solar maximum. In lower latitudes, for example, in central America, evapotranspiration maxima occur even later in the summer (e.g., in August and September) since the amplitude of the seasonal solar cycle is lessened and the accumulation of net irradiance continues through- out the summer. This same effect also is apparent in sub-Saharan Africa and ^South Asia as well as in the Southern Hemisphere. Note the clockwise rotation of phase angles in Brazil, southern Africa and

Australia as the equator is approached. Apparent anomalies arise in steppe or Mediterranean areas (e.g., in northern Libya) since maxima largely depend on moisture, rather than temperature, which may precipitate in but a very few of the winter months. Spring maxima east of the Caspian Sea also result from a shortage of precipitation and subsequently of soil moisture. Evapotranspiration maxima that do not covary with the seasonal maxima of available energy (e.g., air temperature) usually have large soil moisture deficits during part of the year or a nearly constant available energy supply.

Especially in the higher latitudes of the Northern Hemisphere, interpretation of the second evapotranspiration harmonic may seem complex owing to frequent reversals in the phase shift (Figure 3e). It should be remembered, however, that harmonics of frequency two have two maxima separated by six months and, therefore, neighboring grid locations that seem to be out of phase by five to six months are really only out of phase by less than one month. Over much of northern Europe, Asia and North America, therefore, secondary evapotranspiration maxima are evident in June and July. These summer maxima describe an increase in the intensity of the summer evapotranspiration season with latitude—relative to negligible winter evapotranspiration rates. Corresponding maximum phase shifts that occur in December and January (i.e., six months out of phase with the summer maxima) when added to the first harmonic serve to dampen the erroneous, negative winter evapotranspiration rates predicted by the first harmonic. Similar patterns also are apparent in Antarctica. As one moves south from the Northern Hemisphere high latitudes into the mid-latitudes, a counterclockwise rotation of the phase shift is apparent, particularly in the western United States, Europe and western Asia (Figure 3e). This shift represents a lengthening of the evapotranspiration

season owing to the increases in available energy with the decrease in latitude as well as to the marine influence on the western reaches of the continents.

On the eastern portions of North America and Asia, the length of the warm season is affected little by adjacent oceans. Similar patterns exist in the ^Southern ^Hemisphere mid-lati' des, although they are not so well-developed as in the north because of the relatively limited landmass of the mid-latitude Southern Hemisphere.

In the subtropics, a substantial increase of variance with longitude, in both the phase shifts and amplitudes associated with the second harmonic, is apparent (Figure 3e). Over much of north Africa, for example, the seasonal cycle is virtually not present whereas it is exaggerated by the ^Southeast Asian monsoon. The subtropics of the ^Southern ^Hemisphere by contrast exhibit a relatively coherent extension of the evapotranspiration season well into spring and fall. Evapotranspiration in these areas, of course, occurs throughout most of the year.

In much of the tropics, the amplitudes of the second harmonics are smaller than those of their subtropical and mid-latitude counterparts which represent a dampening of the seasonal cycle (Figure 3e). The phase shifts become more variable in an effort to describe a perennial evapotranspiration regime whose maxima often are not well-defined and may be subject more to temporally variable local and mesoscale influences than to the large-scale, solar-forced seasonal cycle. Equatorial South America illustrates this variability, while equatorial Africa portrays a greater degree of coherence because of its lesser topographic variability.

CONCLUDING REMARKS

Using recently available monthly air temperature and precipitation data for the world and an empirically-based water budget algorithm, the large-scale spatial and seasonal variability associated with terrestrial snow cover, soil moisture and evapotranspiration have been estimated and inductively evaluated. Even though we regard these findings as a zeroth-order approximation--one of a very few available, these data provide both empirically-based climate fields to which general circulation results can be compared and realistic initial fields that may be used in GCM seasonal cycle experiments.

Of the three climate fields presented, the seasonal snow cover cycle exhibits the greatest statistical regularity, particularly in the higher latitudes of the Northern Hemisphere. In the mid-latitudes, on the other hand, the seasonal snow cover as well as its albedo and water equivalent can be highly variable, both spatially and temporally. As snow has a high albedo and the water entrained in the snowpack is a potentially significant source of soil moisture (especially during the melt season which closely precedes the growing season) these results suggest that the interrelationships between the seasonal snow cycle and large-scale atmosphere circulation need to be well-represented within GCMs. For a number of reasons, it is not sufficient to designate snow cover as either present or absent. The seasonally transient water contained in the snowpack, for example, has an important influence on the surface energy balance through latent flux which derives from melt water; that is, snow cover has climatic significance beyond its obvious effect on regional albedo. The magnitude of the snow water store, in fact, can be as large as or larger than the soil moisture store. Since the influence of snow and snow water equivalent on climate is affected by topographic and vegetational factors which have not

been considered here, further research into the large-scale role which the terrestrial snow cycle plays in the seasonal climate cycle is required. It is known, for example, that the regional albedo of a snow covered forest is substantially less than a snow covered grassland (Leonard and Eschner, 1968) which, of course, directly affects the surface energy balance. The differential melt and subsequent soil moisture responses of seasonally snow covered forests and grasslands as well as ensuing effects on the large scale circulation of the atmosphere are not so well-known. It is likely that more detailed representations of the seasonal snow cycle will unveil more realistic but even more variable snow cover and snow water equivalent fields. ←

Terrestrial soil moisture is much more temporally and spatially variable than snow cover or snow water equivalent because of its greater dependence upon the ensemble of local environmental factors. A number of large-scale patterns are evident, however, ^{they} can be explained by accepted climate principles. The mid- to high latitudes of the Northern Hemisphere, for example, reach peak soil moistures after the snow accumulation season during the spring thaw while soil moisture in near monothermal tropics follows the seasonal rainfall cycle. Even though our maps suggest that the seasonal soil moisture cycle is highly variable, it is probable that more realistically-derived fields that account for soil, vegetational and physiographic variables will exhibit even greater variability. ←

Future representations of terrestrial soil moisture, as a consequence, should include more of the salient near-surface environmental and hydrologic variables.

Seasonal evapotranspiration has less spacio-temporal variability than soil moisture but more than snow cover. The former is principally due to the observation that evapotranspiration is relatively insensitive to changes in soil moisture until soil moisture level falls well-below one-half the field capacity (e.g.,

see Mather, 1974; 106; Nappo, 1975). Once again, our characterization may be oversimplified, since the vegetation structure and morphology as well as physiographic and pedological considerations are absent.

Because the spacio-temporal variability of evapotranspiration has key importance for the general circulation of the atmosphere (Mintz, 1982), the relationships between the terrestrial biosphere and the near-surface atmosphere should be modeled in greater detail (Mintz et al., 1983). At the same time, empirically-derived evapotranspiration climatologies must be improved, most likely through remote sensing means. Nevertheless, the physical expectation of the macro- and mesoscale features of the terrestrial seasonal evapotranspiration cycle (e.g., evapotranspiration follows available energy except in areas that are seasonally or annually water-limited) seems to be reasonably well-represented in this climatology of evapotranspiration.

ACKNOWLEDGEMENTS

Financial support (NASA Grant number NAG 5-107) from the Laboratory for Atmospheric Sciences at NASA's Goddard Space Flight Center in Greenbelt, Maryland is most gratefully acknowledged.

REFERENCES

- Anderson, E. A. 1973. National Weather Service River Forecast System-Snow Accumulation and Ablation Model. Silver Spring, Maryland: NWS, USDOC (NOAA Tech. Memo. NWS HYDRO-17), 217 pgs.
- Baumgartner, A. 1981. 'Water Balance'. Paper presented at the JSC Study Conference on Land Surface Processes in Atmospheric General Circulation Models. Greenbelt, Maryland: NASA, Goddard Space Flight Center.
- Carson, D. L. 1981. 'Current Parameterizations of Land-Surface Processes in Atmospheric General Circulation Models'. Paper presented at the JSC Study Conference on Land Surface Processes in Atmospheric General Circulation Models. Greenbelt, Maryland: NASA, Goddard Space Flight Center.
- Davies, J. A. and C. D. Allen. 1973. 'Equilibrium, Potential and Actual Evaporation from Cropped Surfaces in Southern Ontario'. Journal of Applied Meteorology, 12, 649-657.
- Dewey, K. F. and R. Heim, Jr. 1981. Satellite Observations of Variations in Northern Hemisphere Seasonal Snow Cover. Washington, D.C.: National Earth Satellite Service, NOAA/USDOC. (NOAA Tech. Rep. NESS 87).
- Dickinson, R. E. 1983. 'Land Surface Processes and Climate--Surface Albedos and Energy Balance'. Advances in Geophysics, 25, 305-353.
- Jaeger, L. 1976. Monatskarten des Niederschlages für die ganze Erde. Berichte Deutscher Wetterd. NR. 139, Offenbach.
- Jaeger, L. 1983. 'Monthly and Areal Patterns of Mean Global Precipitation' in Street-Perrott, A. et al. (eds.). Variations in the Global Water Budget. Dordrecht, Holland: D. Reidel, 129-140.
- Jensen, M. E. (ed.) 1973. Consumptive Use of Water and Irrigation Water Requirements. New York: American Society of Civil Engineers. 215 pgs.
- Kotliakov, V. M. and A. N. Krenke. 1981. 'The Data on Snow Cover and Glaciers for the Global Climatic Models' paper presented at the JSC Study Conference on Land Surface Processes in Atmospheric General Circulation Models. Greenbelt, Maryland: NASA Goddard Space Flight Center. ←
- Lee, R. 1978. Forest Microclimatology. New York: Columbia University Press. 276 pgs.
- Leonard, R. E. and A. R. Eschner. 1968. 'Albedo of Intercepted Snow'. Water Resources Research. 4, 931-935.
- Mather, J. R. 1974. Climatology: Fundamentals and Applications. New York: McGraw-Hill. 412 pgs.
- Mintz, Y. 1982. The Sensitivity of Numerically Simulated Climates to Land-Surface Boundary Conditions. Greenbelt, Maryland: NASA, Goddard Space Flight Center (NASA Tech. Memo. 83985).

- Mintz, Y., P. J. Sellers and C. J. Willmott. 1983. On the Design of an Interactive Biosphere for the GLAS General Circulation Model. Greenbelt, Maryland: NASA, Goddard Space Flight Center (NASA Tech. Memo. 84973).
- Möller, F. 1951. 'Vierteljahreskarten des Niederschlages'. Petermanns Geogr. Mitt., 95, 1-7.
- Nappo, C. J. 1975. 'Parameterization of Surface Moisture and Evaporation Rate in a Planetary Boundary Layer Model'. Journal of Applied Meteorology, 14, 289-296.
- Pysklywec, D. W., K. S. Davar and D. I. Bray. 1968. 'Snowmelt at an Index Plot'. Water Resources Research. 4, 937-946.
- Sellers, P. J. 1981. Vegetation Type and Catchment Water Balance. Leeds: Leeds University, Dept. of Geography (Ph. D. Thesis). 836 pgs.
- Steinhauser, F. (Tech. Supervisor). 1979. Climatic Atlas of North and Central America. I: Maps of Mean Temperature and Precipitation. Geneva: WMO (also UNESCO and Cartographia).
- Storr, D. 1978. A Comparison of Daily Snowmelt Calculated by the U.S. Corps of Engineers Theoretical Model with Measured Amounts on a Snowpillow. Ganges; British Columbia: Storm Water Resources Consulting Service.
- Thorntwaite, C. W. 1948. 'An Approach Toward a Rational Classification of Climate'. Geographical Review. 38, 55-94.
- Thorntwaite, C. W. and B. Holzman. 1939. 'The Determination of Evaporation From Land and Water Surfaces'. Monthly Weather Review. 67, 4-11.
- Willmott, C. J. 1977. WATBUG: A Fortran IV Algorithm for Calculating the Climatic Water Budget. Elmer, New Jersey (Publications in Climatology, Vol. 30, No. 2).
- Willmott, C. J. 1984a. 'Models Climatic' in Oliver, J. E. (ed.). Encyclopedia of Climatology. Stroudsburg, Pennsylvania: Hutchinson Ross. In press.
- Willmott, C. J. 1984b. 'On the Evaluation of Model Performance in Physical Geography' in Gaile, G. L. and C. J. Willmott (eds.). Spatial Statistics and Models. Dordrecht, Holland: D. Reidel, 443-460.
- Willmott, C. J., J. R. Mather and C. M. Rowe. 1981. Average Monthly and Annual Surface Air Temperature and Precipitation Data for the World. Part 1: The Eastern Hemisphere. Part 2: The Western Hemisphere. Elmer, New Jersey: C. W. Thorntwaite Associates (Publications in Climatology, Vol. 34, Nos. 1 and 2).
- Willmott, C. J., C. M. Rowe and W. D. Philpot. 1984. 'Small-scale Climate Maps: A Sensitivity Analysis of Some Common Assumptions Associated with Grid Point Interpolation and Contouring'. Annals of the Association of American Geographers. Submitted.

FIGURE CAPTIONS

Figure 1 Based upon seasonally representative, mid-monthly estimates of snow water equivalent at the nodes of a 4° of latitude by 5° of longitude lattice, maps (a) and (b) are isoline representations of the means and standard deviations, respectively, associated with the seasonal cycles at the grid points. The variances contained within the grid point seasonal cycles were harmonically decomposed and, for all grid points, the roots of the variances left unexplained by the first two harmonics (i.e., the errors) were contoured and are presented in map (c). Maps (d) and (e) give the spatial distributions of the amplitudes (lengths of the arrowed vectors) and phase shifts (direction of the arrow heads) associated with the first and second harmonics, respectively.

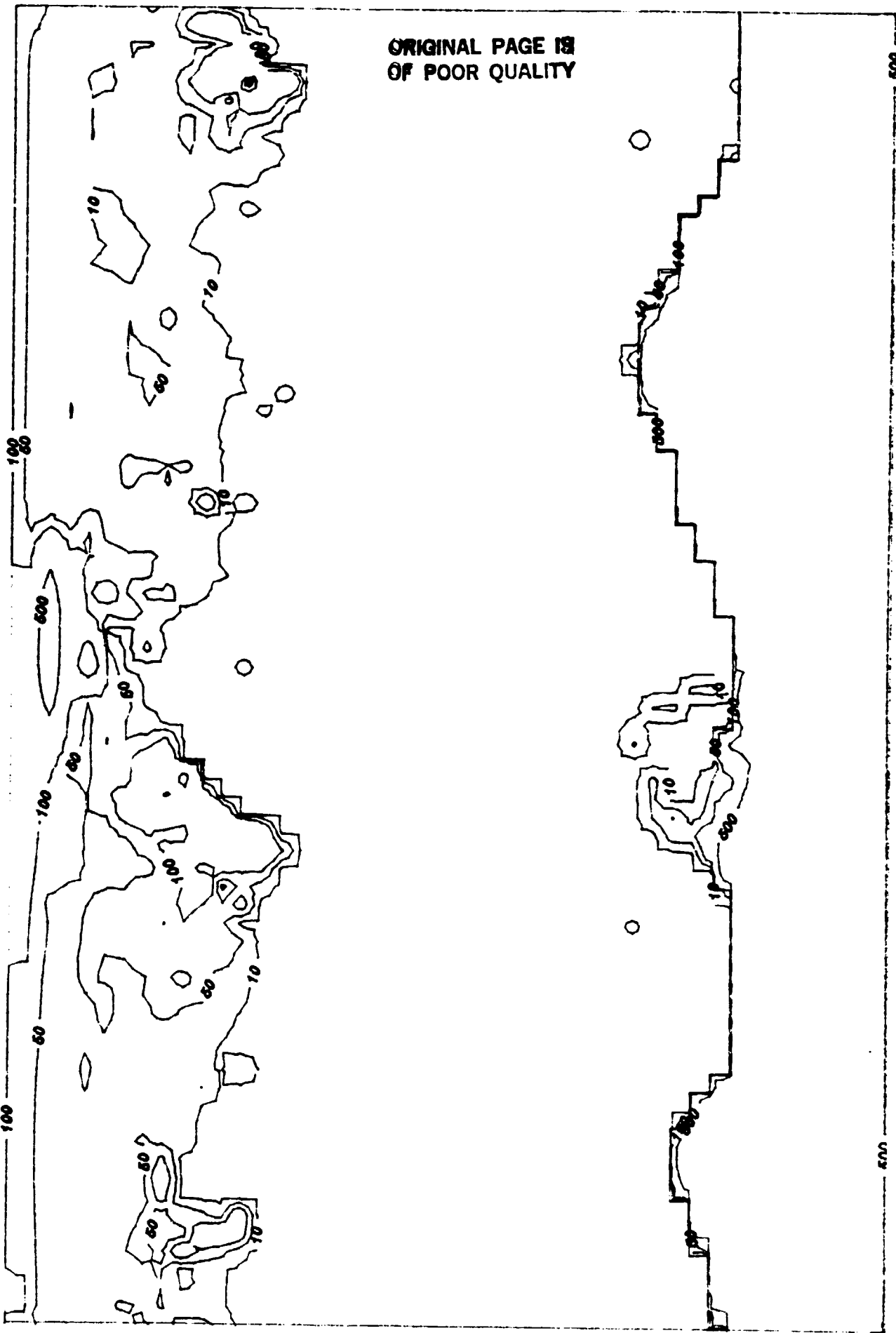
Figure 2 Based upon seasonally representative, mid-monthly estimates of ^{soil moisture}~~evapotranspiration~~ at the nodes of a 4° of latitude by 5° of longitude lattice, maps (a) and (b) are isoline representations of the means and standard deviations, respectively, associated with the seasonal cycles at the grid points. The variances contained within the grid point seasonal cycles were harmonically decomposed and, for all grid points, the roots of the variances left unexplained by the first two harmonics (i.e., the errors) were contoured and are presented in map (c). Maps (d) and (e) give the spatial distributions of the amplitudes (lengths of the arrowed vectors) and phase shifts (direction of the arrow heads) associated with the first and second harmonics, respectively.

Figure 3 Based upon seasonally representative, mid-monthly estimates of ~~soil moisture~~^{evapotranspiration} at the nodes of a 4° of latitude by 5° of longitude ←
lattice, maps (a) and (b) are isoline representations of the means and standard deviations, respectively, associated with the seasonal cycles at the grid points. The variances contained within the grid point seasonal cycles were harmonically decomposed and, for all grid points, the roots of the variances left unexplained by the first two harmonics (i.e., the errors) were contoured and are presented in map (c). Maps (d) and (e) give the spatial distributions of the amplitudes (lengths of the arrowed vectors) and phase shifts (direction of the arrow heads) associated with the first and second harmonics, respectively.

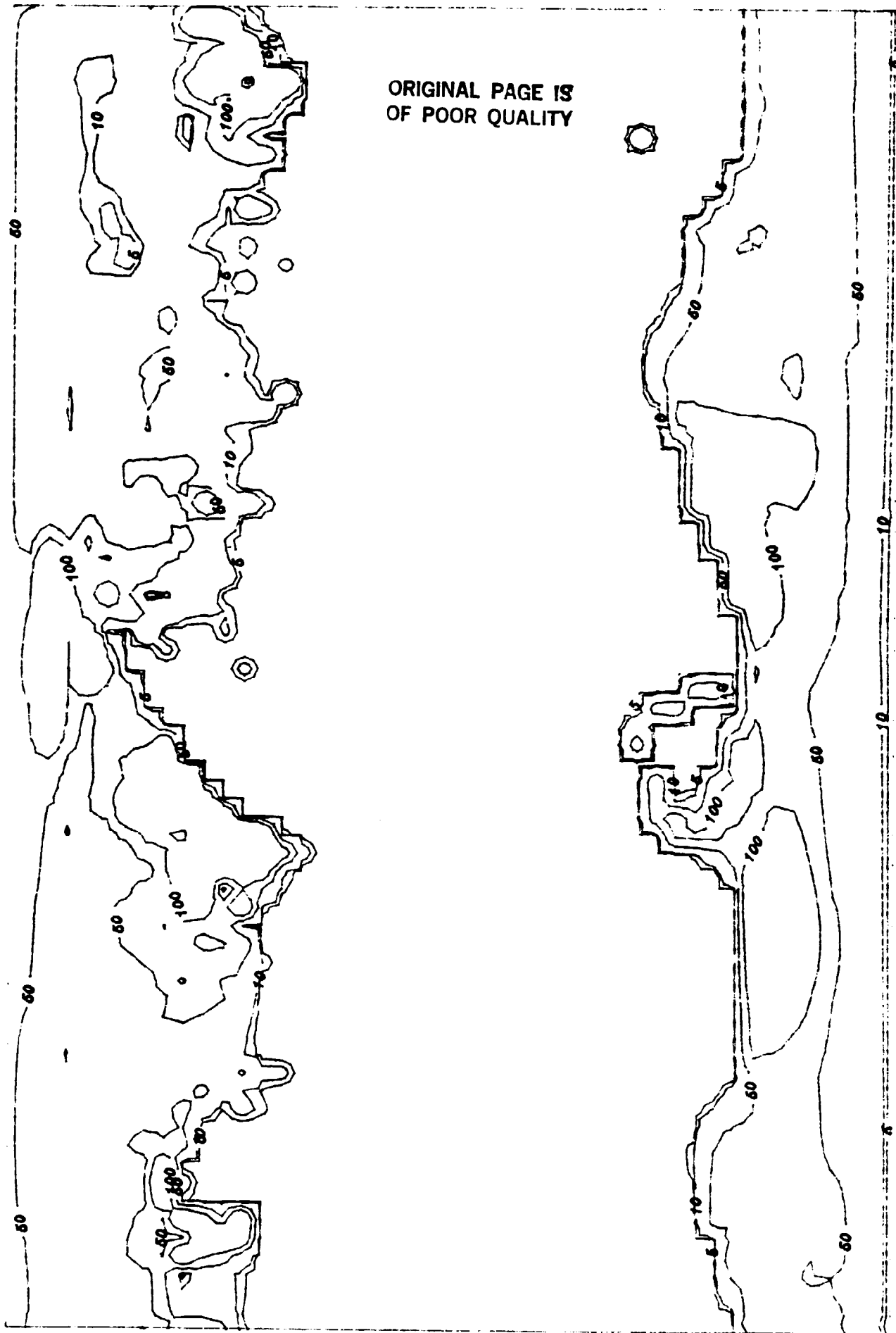
FIGURE TITLES

- Figure 1 Seasonal Water Equivalent of the Snowpack
- a) Annual Average (mm)
 - b) Seasonal Standard Deviation (mm)
 - c) Root of the Variance Unexplained by the First Two Harmonics (mm)
 - d) Amplitude (mm) and Phase Angle of the First Harmonic
 - e) Amplitude (mm) and Phase Shift of the Second Harmonic
- Figure 2 Seasonal Soil Moisture
- a) Annual Average (mm)
 - b) Seasonal Standard Deviation (mm)
 - c) Root of the Variance Unexplained by the First Two Harmonics (mm)
 - d) Amplitude (mm) and Phase Angle of the First Harmonic
 - e) Amplitude (mm) and Phase Shift of the Second Harmonic
- Figure 3 Seasonal Evapotranspiration
- a) Annual Average (mm/month)
 - b) Seasonal Standard Deviation (mm/month)
 - c) Root of the Variance Unexplained by the First Two Harmonics (mm/month)
 - d) Amplitude (mm/month) and Phase Angle of the First Harmonic
 - e) Amplitude (mm/month) and Phase Shift of the Second Harmonic

Mean Snow Cover

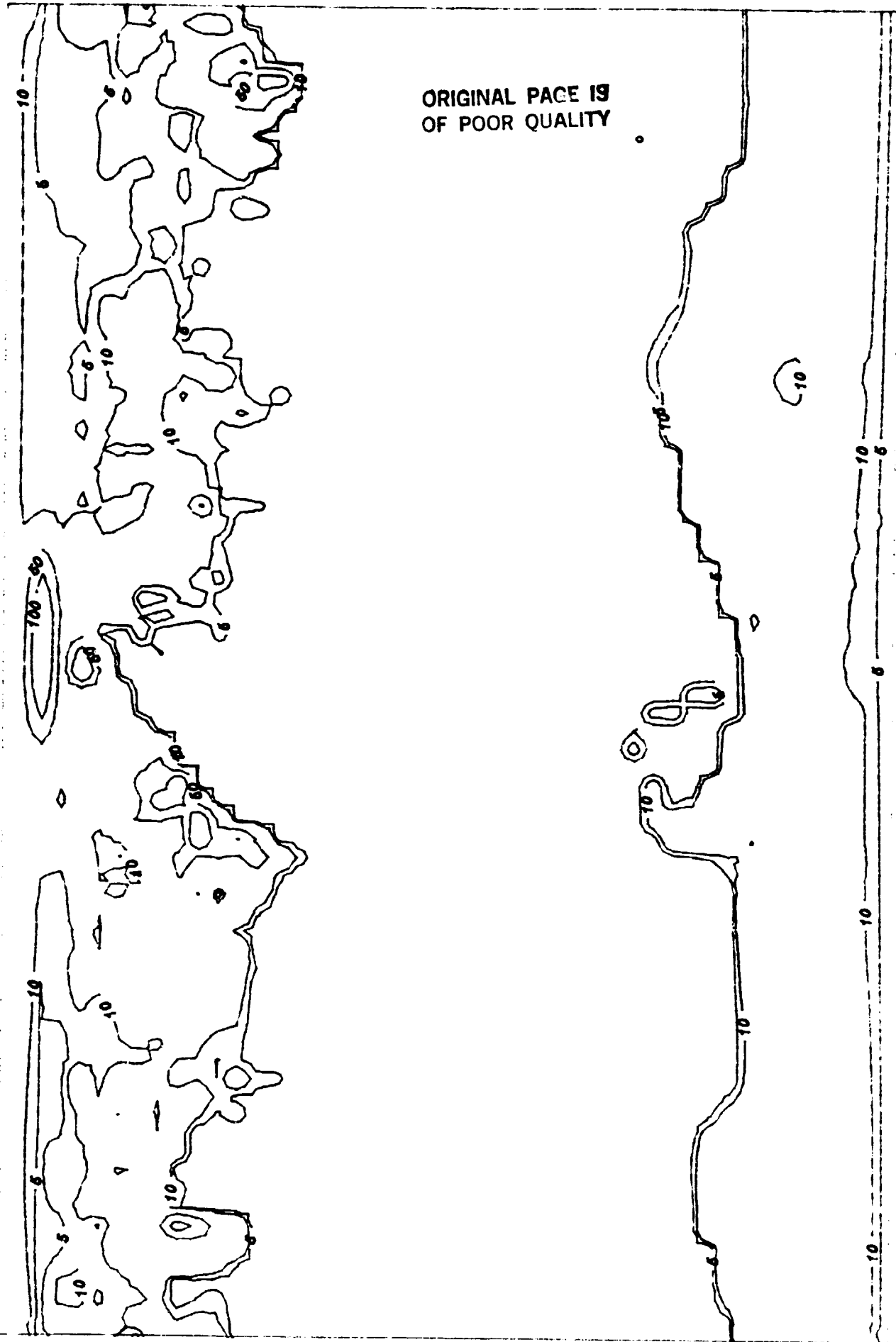


Snow Cover Standard Deviation



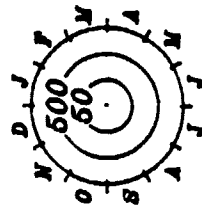
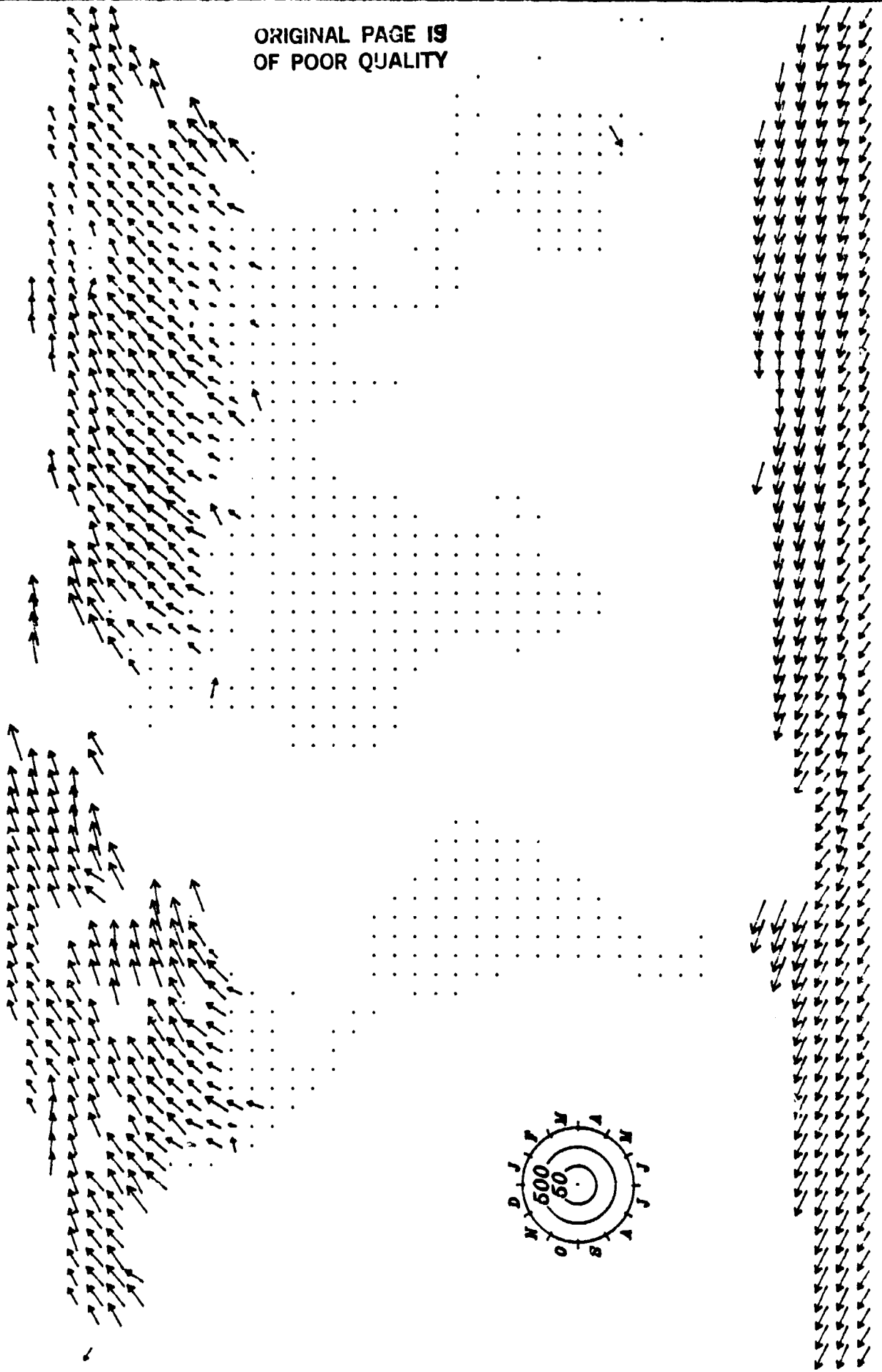
ORIGINAL PAGE IS
OF POOR QUALITY

Snow Cover Error



Snow Cover First Harmonic

ORIGINAL PAGE IS
OF POOR QUALITY



Snow Cover Second Harmonic

ORIGINAL PAGE IS
OF POOR QUALITY

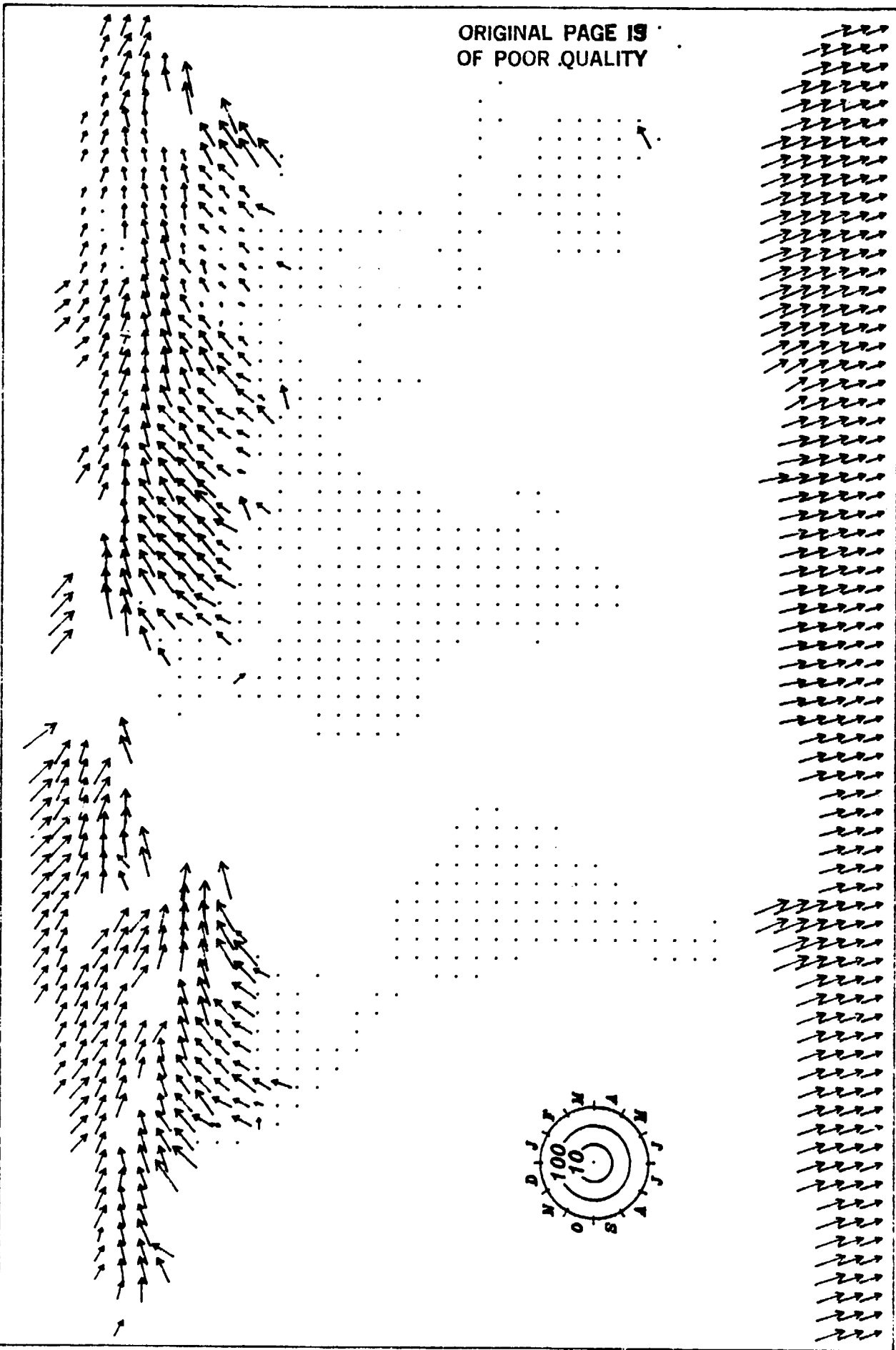
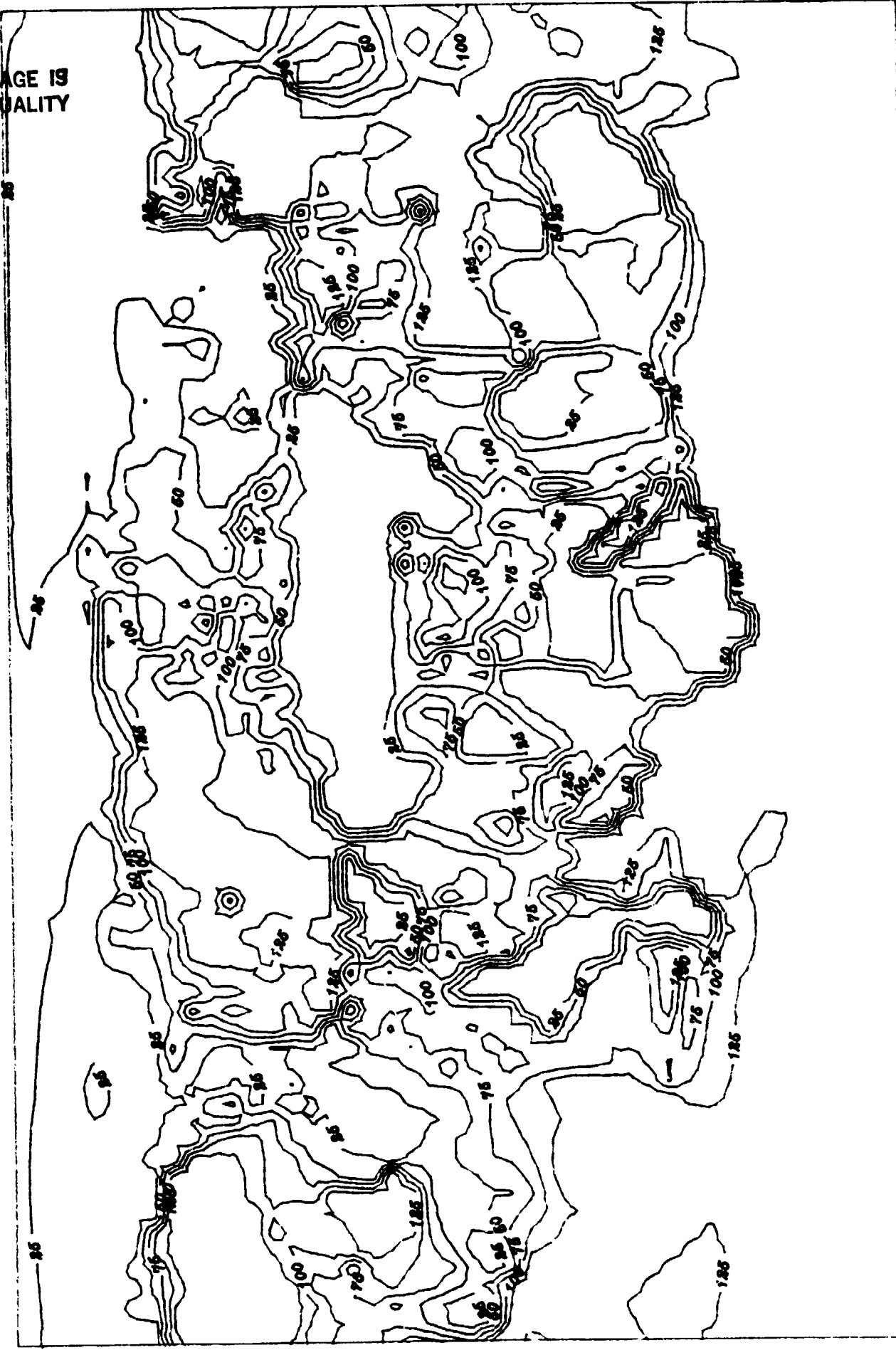
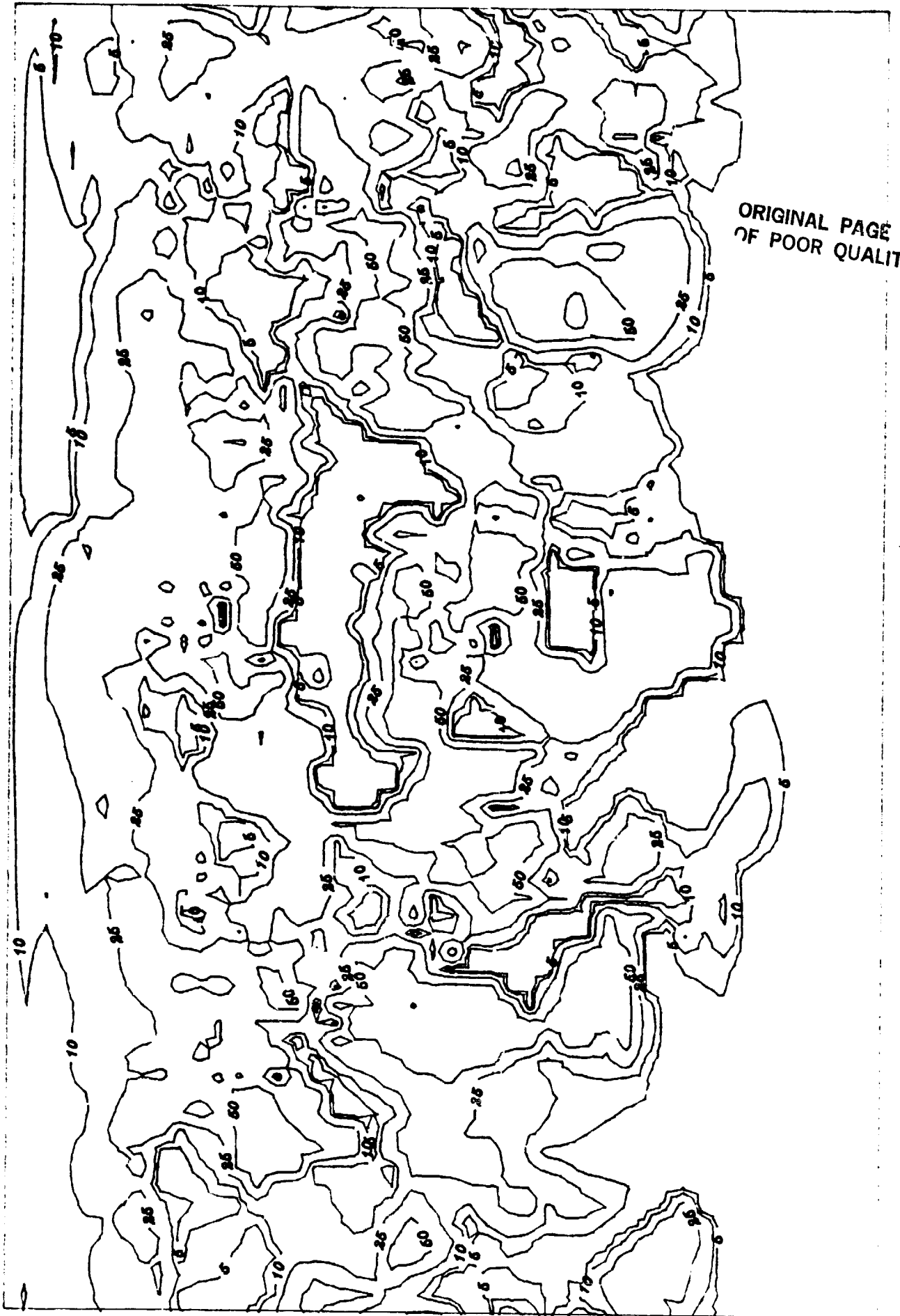


Fig. 812

Mean Annual Soil Moisture



Soil Moisture Standard Deviation



ORIGINAL PAGE IS
OF POOR QUALITY

ORIGINAL PAGE IS
OF POOR QUALITY

Soil Moisture Error

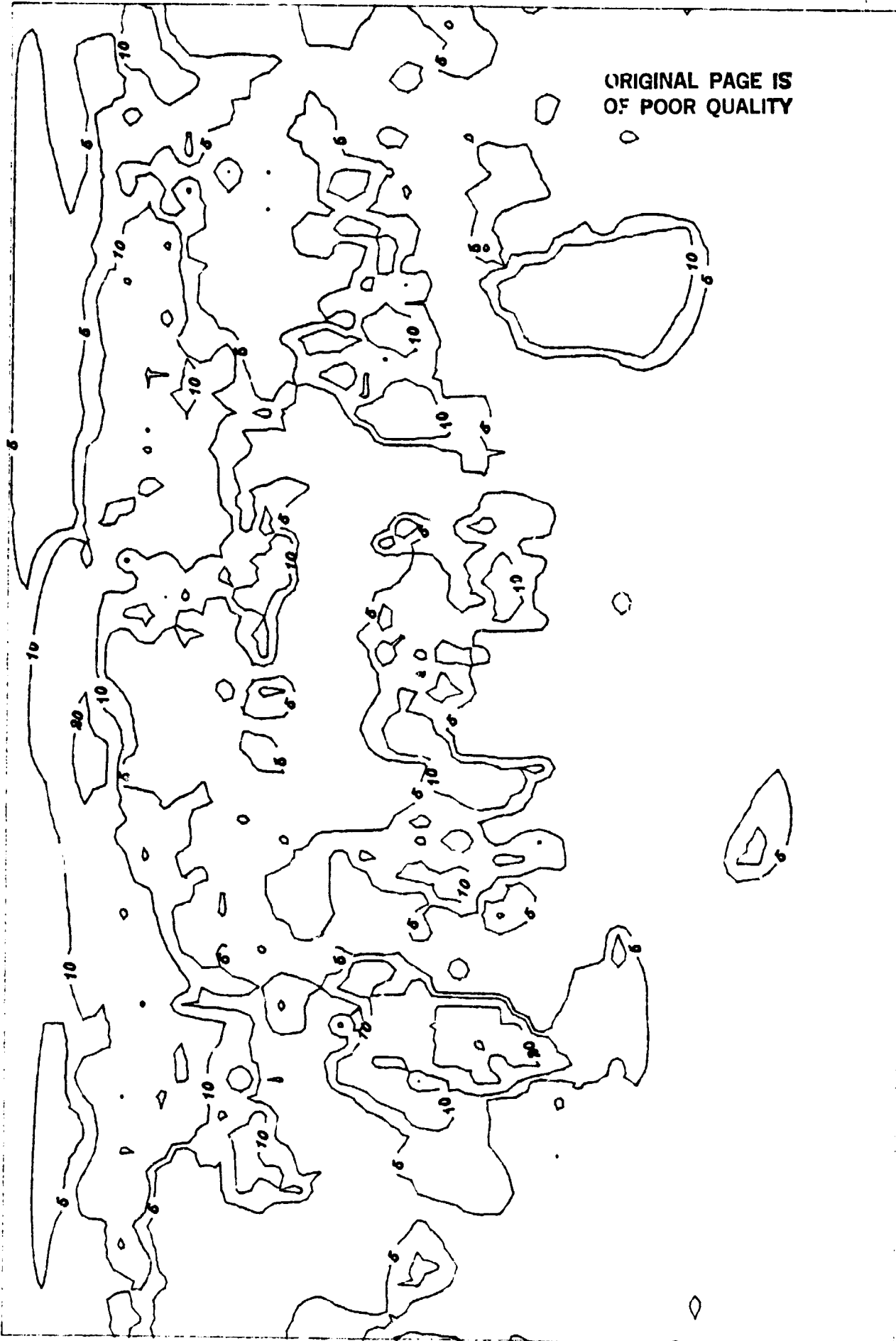
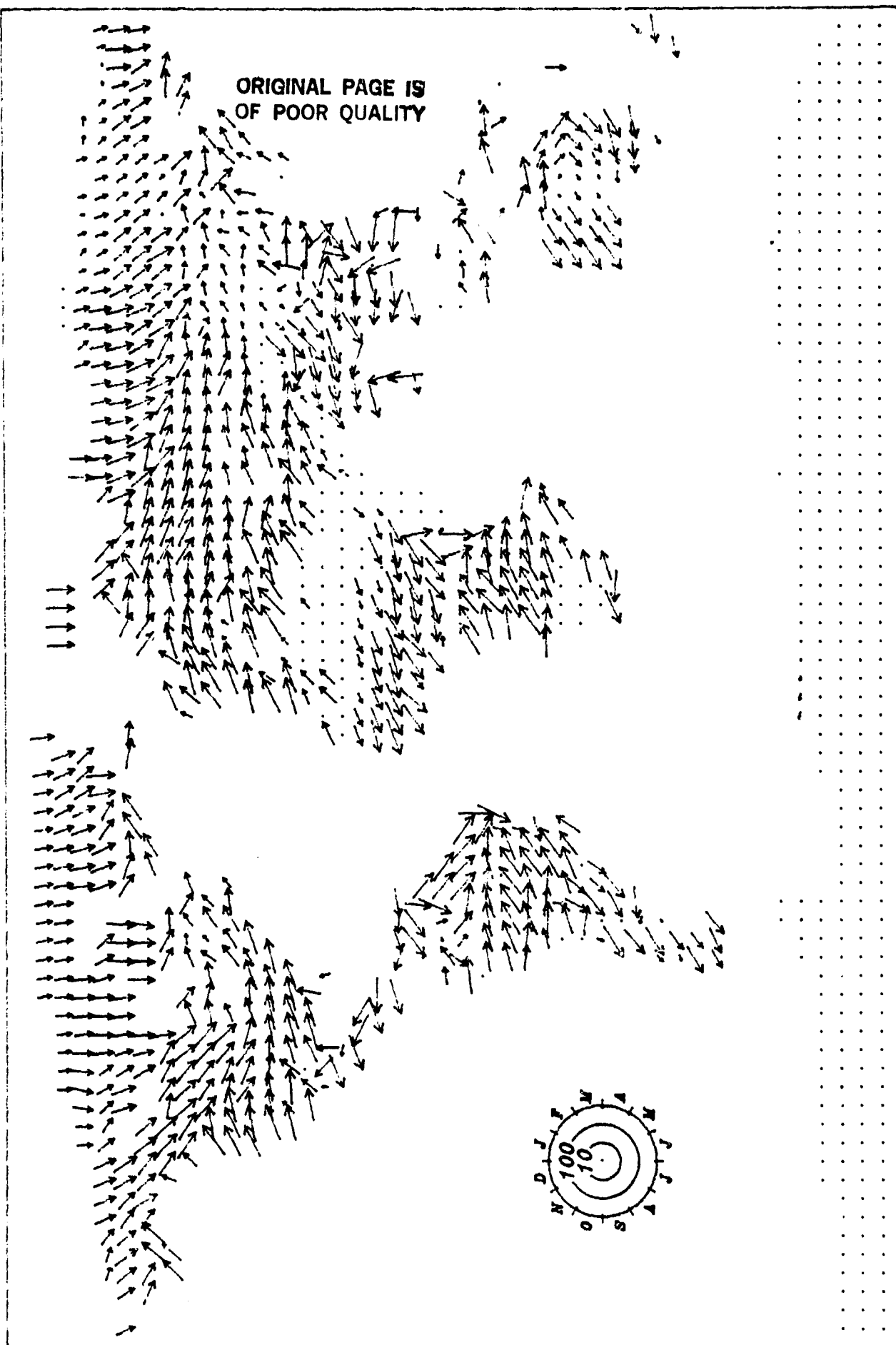


Fig. 82c

Soil Moisture First Harmonic

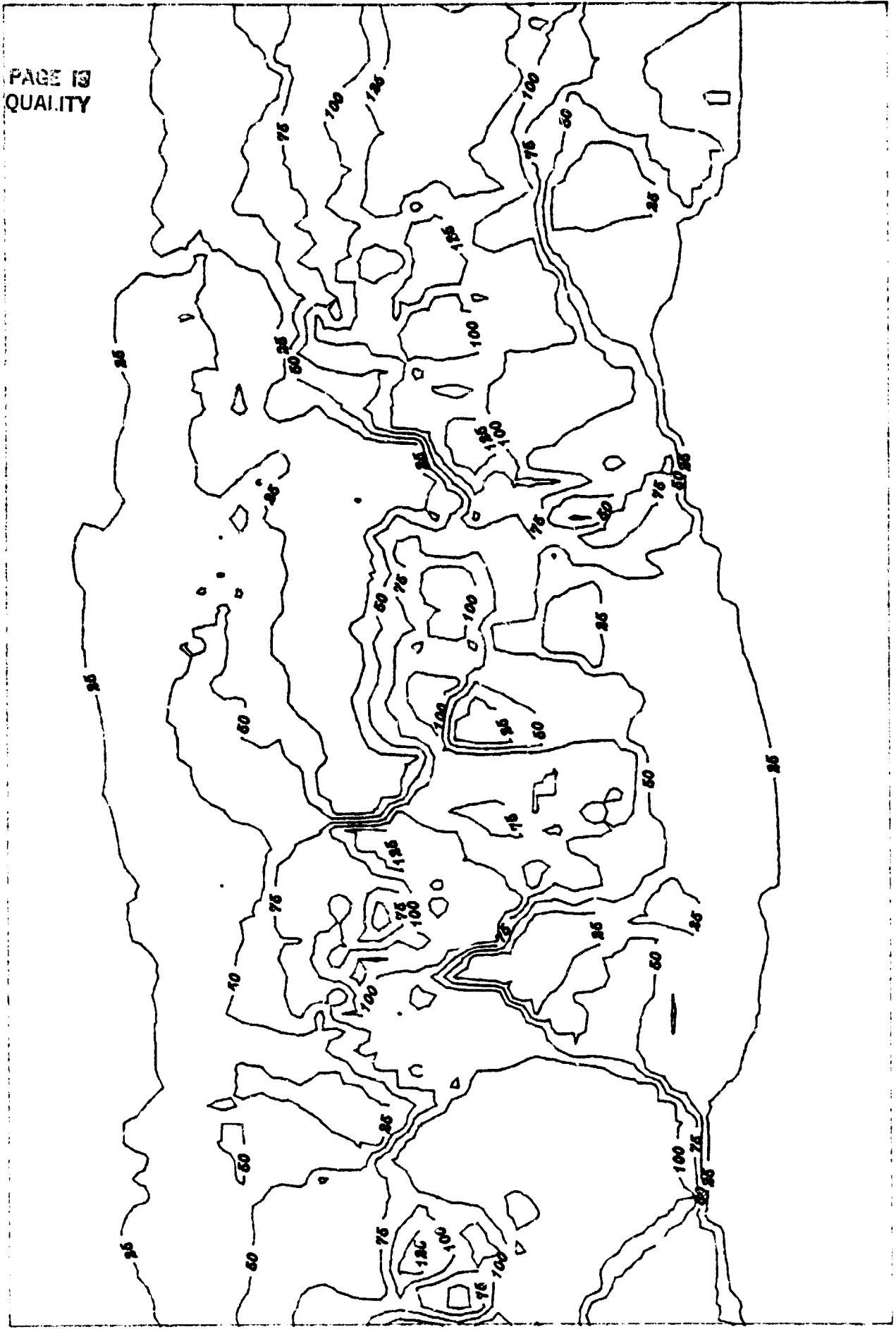


Soil Moisture Second Harmonic

ORIGINAL PAGE IS
OF POOR QUALITY

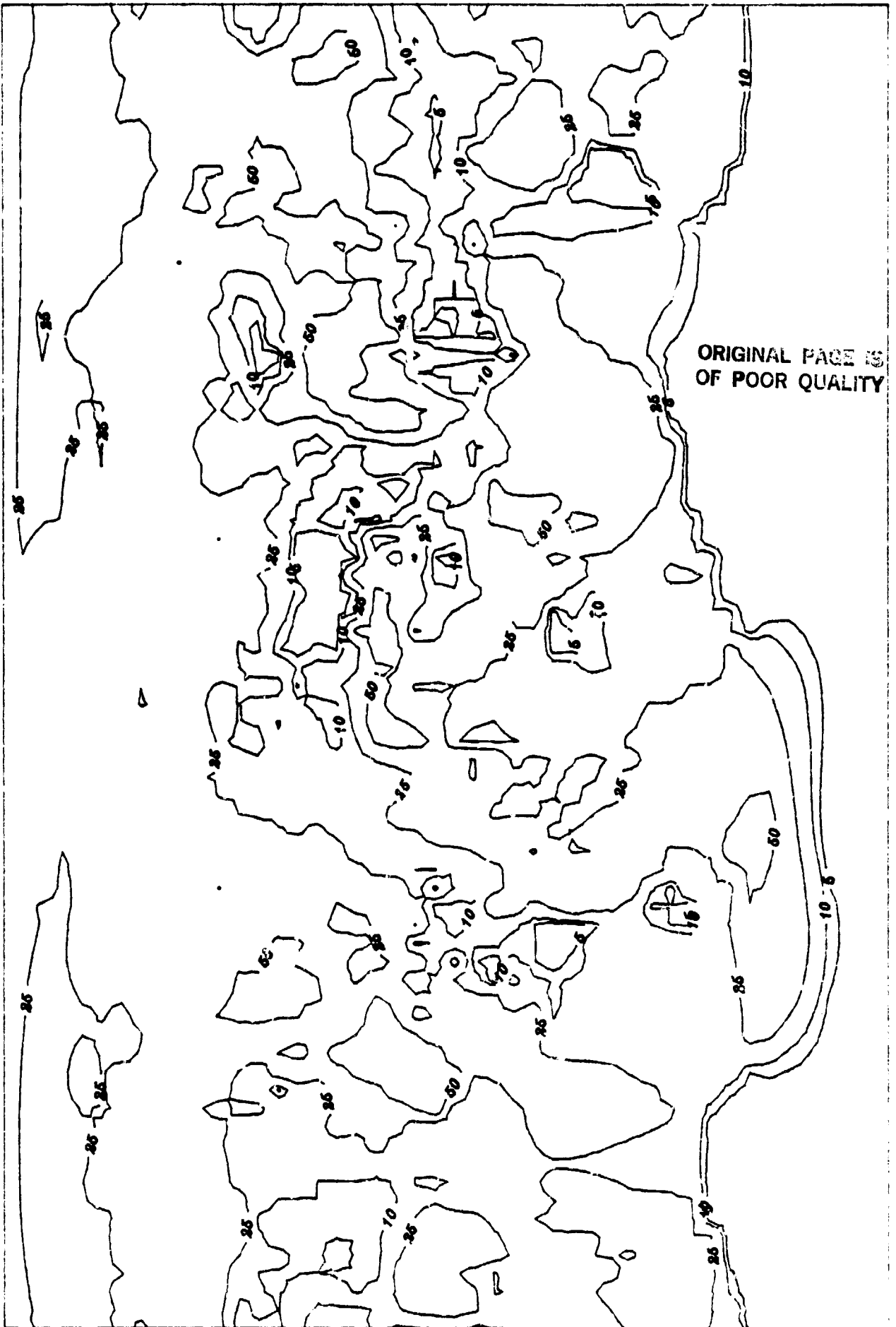


Mean Annual Evapotranspiration



13

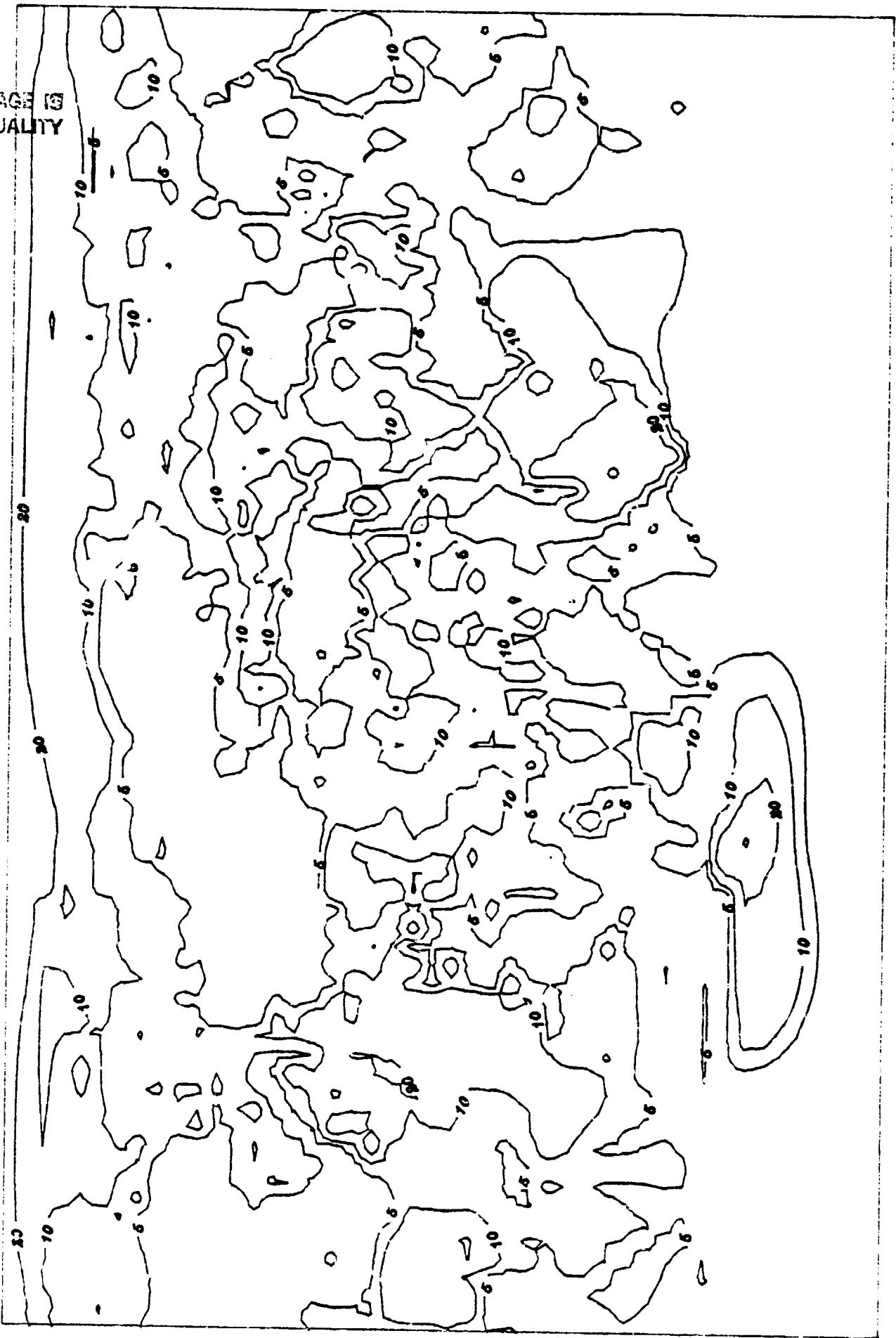
Evapotranspiration Standard Deviation



ORIGINAL PAGE IS
OF POOR QUALITY

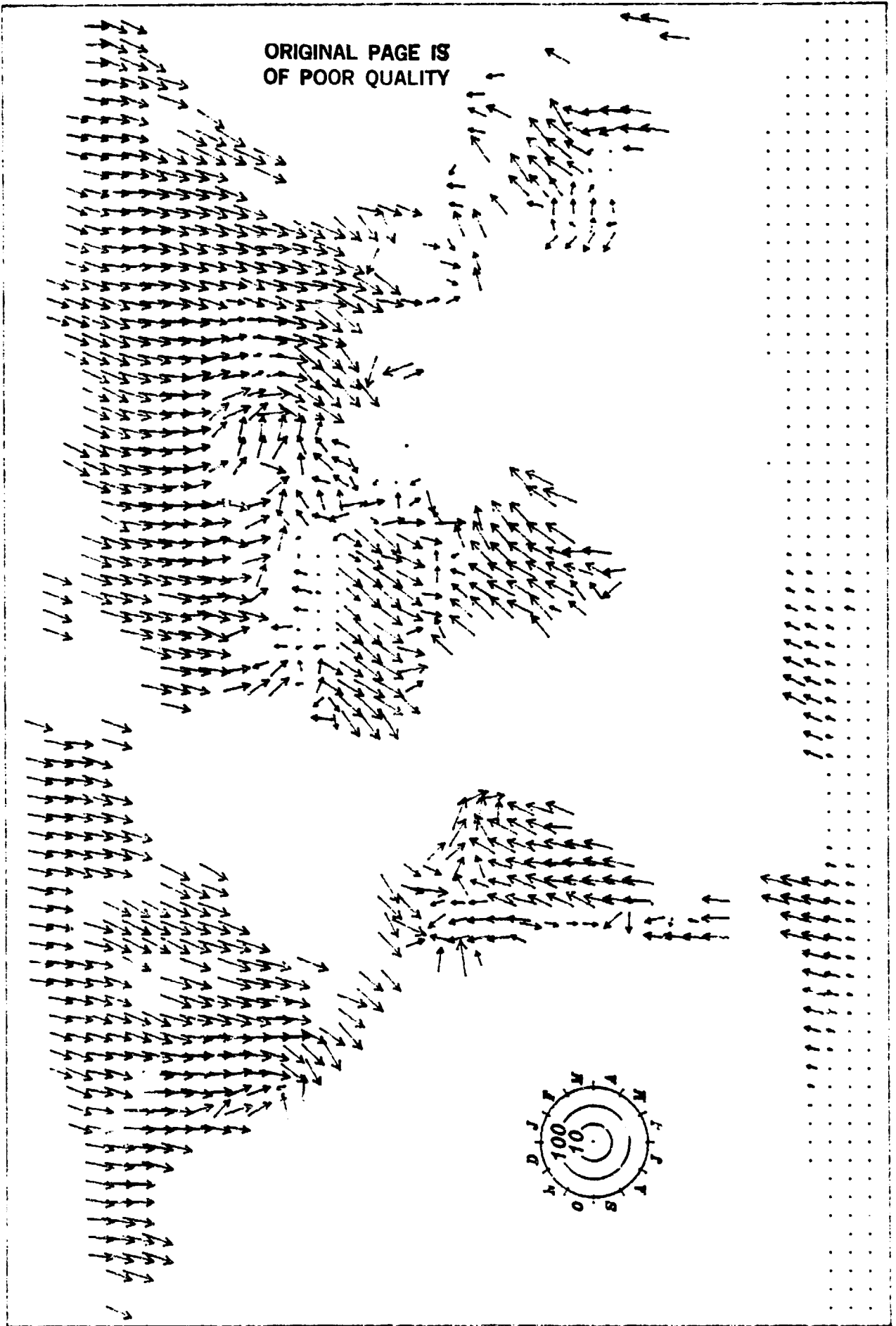
ORIGINAL PAGE IS
OF POOR QUALITY

Evapotranspiration Error



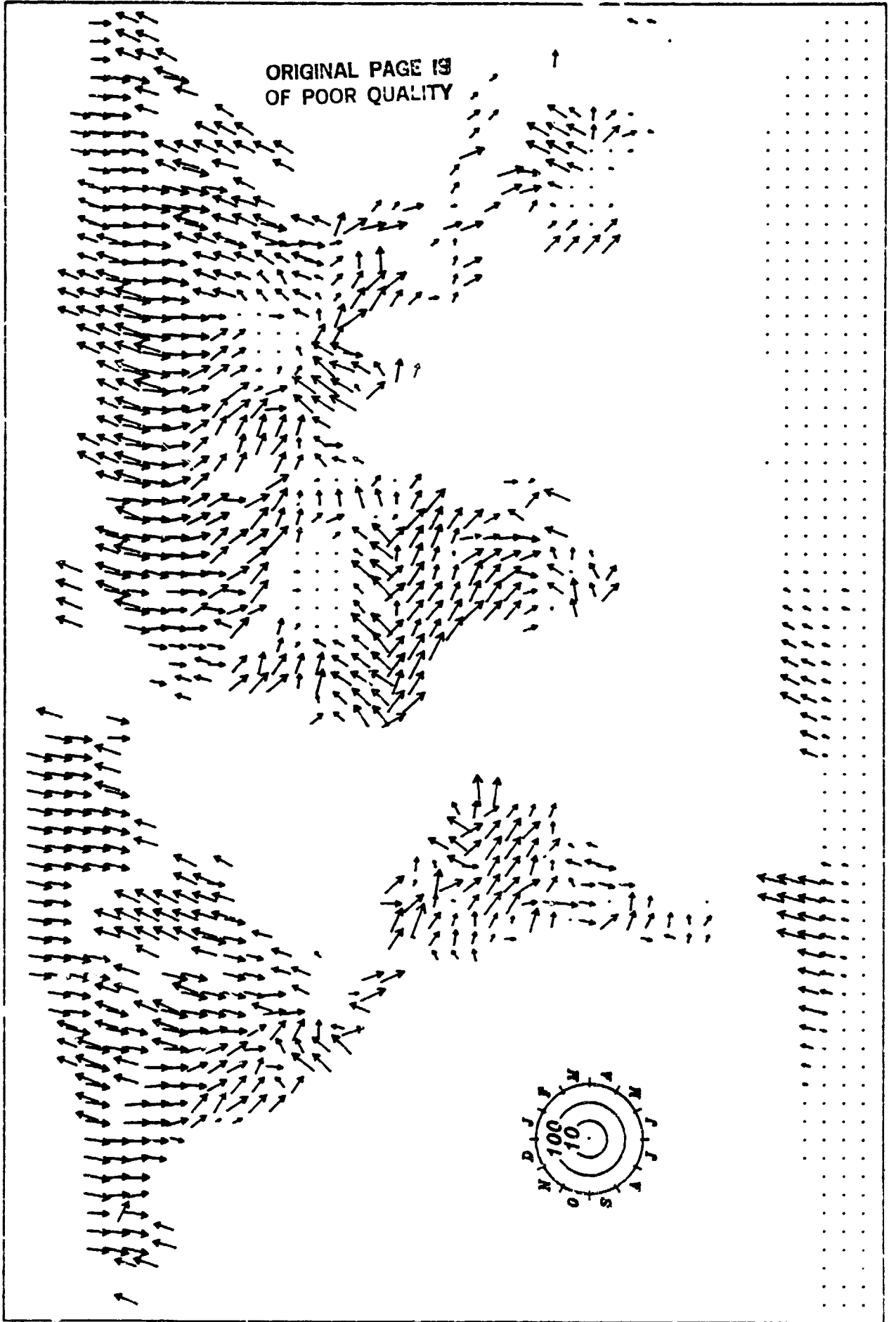
15 18 30

Evapotranspiration, First Harmonic



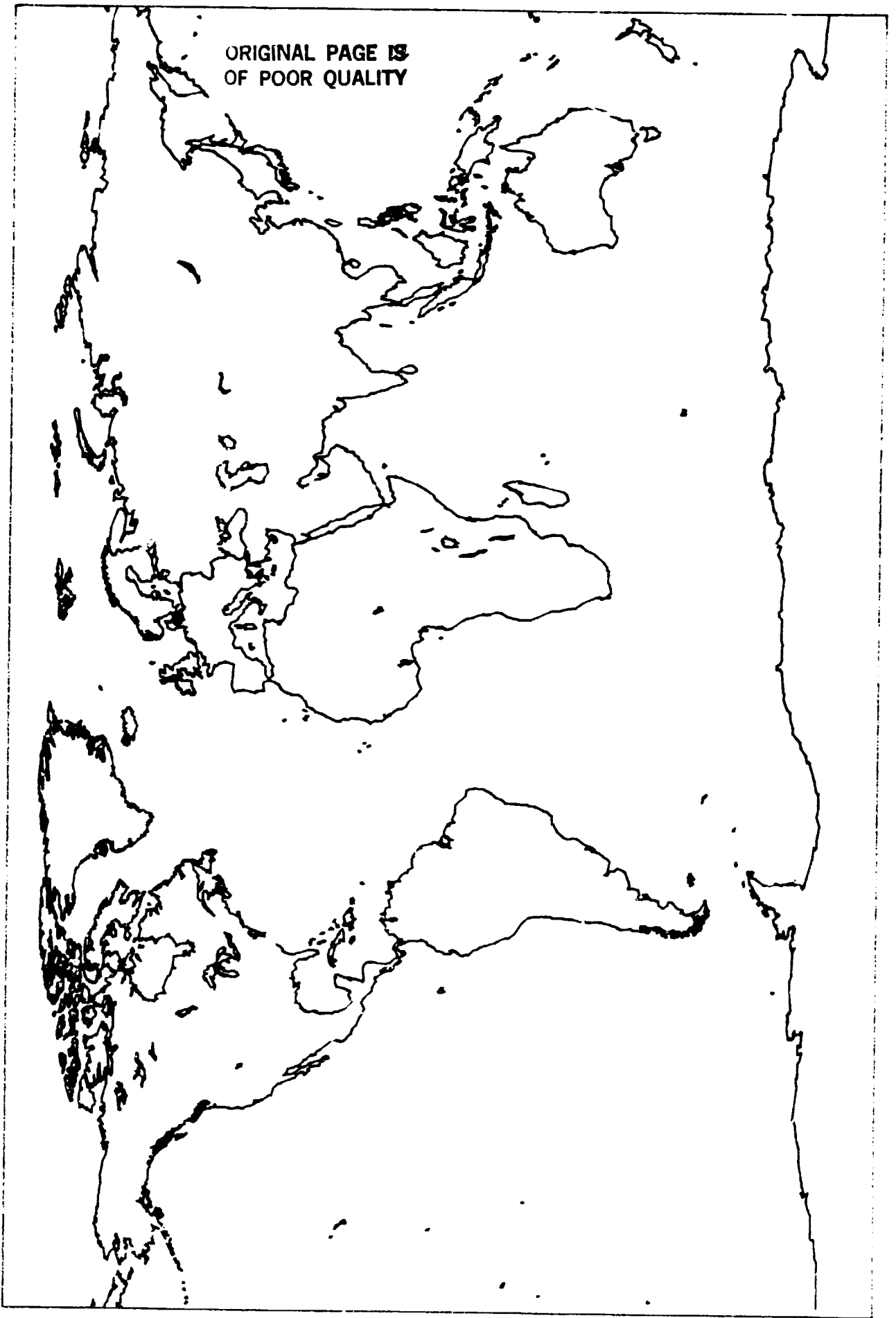
Evapotranspiration Second Harmonic

ORIGINAL PAGE IS
OF POOR QUALITY



13/30

ORIGINAL PAGE IS
OF POOR QUALITY



APPENDIX 3

Evaluation of Thornthwaite's Model Through
Comparisons with Lettau's Model.

EVALUATION OF THORNTHWAITE'S MODEL THROUGH COMPARISONS WITH LETTAU'S MODEL

Phase three of the project called for an evaluation of the Thornthwaite model of actual evapotranspiration under climatic conditions where it is felt to provide questionable results. In addition, the model is often validated by comparing measured stream runoff with that predicted by the model. Discrepancies between the time series of calculated and predicted runoff are reduced by adjusting the soilwater holding capacity or the β function. Although one might assume that the resulting soil moisture time series is correct, this procedure may produce compensating errors in evapotranspiration and soil moisture storage. It is therefore desirable to validate Thornthwaite's model determinations of actual evapotranspiration and soil moisture in a variety of climates.

For example, for the Maurice River basin in southern New Jersey, during the years 1950-1956, the total precipitation was 8204 mm (1172 mm/yr) and the total measured runoff was 3398 mm (per unit area). Assuming that the net change in water storage over these seven years is negligible and that there is no subterranean discharge from the basin, the total evapotranspiration for the period is 4806 mm. On the other hand, the total evapotranspiration calculated by the Thornthwaite model for the period depends on the assumed value of the model soil moisture storage. With an assumed value of storage of 25 mm, the accumulated evaporation is 4337 mm. Increasing the assumed storage to 225 mm increases the accumulated evapotranspiration to 4781 mm. The smaller value is 10% below the difference between precipitation and runoff.

In the case of a dryer climate, for the experimental agricultural watershed #1111 in Chikasha, Oklahoma during the years 1962-1972 there was an accumulated precipitation of 6151 mm (599 mm/yr), and a runoff of 200 mm giving an accumulated evapotranspiration of 5951 mm. Accumulated evapotrans-

piration for this site according to the Thornthwaite method varies from 5662 mm when a storage of 125 is assumed to 5978 mm for a storage of 250 mm. The former is 5% below the difference of the accumulated precipitation and runoff.

In addition, it is known that the Thornthwaite method underestimates cold season evapotranspiration. Therefore, if the accumulated amount is adjusted to agree with accumulated precipitation less accumulated runoff, it must over estimate warm season evapotranspiration by an equivalent amount.

The most frequent means for checking model performance has been to compare the model with lysimeter observations of actual evapotranspiration. Such an approach is not satisfactory for a study involving large areas of landscape because of the impossibility of relating lysimeter measurements, usually of a single agricultural crop, to the evaporation from deep rooted, often forested, vegetation. Uncertainty is increased by the heterogeneous character of plant soil and terrain features found in extended real landscapes.

A possible means for checking the Thornthwaite model has been suggested by an approach developed by Lettau (1969) and Lettau (personal communication) and developed by Lettau and Baradas (1973), Lettau, Lettau and Molion (1979). The aim is to explore the possibility that this model can be calibrated against actual watershed measurements to derive the seasonal time series of actual evapotranspiration and soil moisture. Lettau's Model is developed from a water budget equation

$$P = N + E + \frac{\delta m}{\delta t} \quad (5)$$

where P, N, and E are the fluxes of precipitation, runoff and evapotranspiration per unit area per unit of time (t) (day, month, year, etc). Moisture, m, is the exchangeable moisture stored anywhere in the soil, whether in the root zone or not, so long as it is subject to eventual removal from the stream basin.

Equation (5) is parameterized by dividing runoff and evapotranspiration into components which occur in the same time interval in which the rainfall

occurs (called immediate runoff and evapotranspiration and designated by single primes) and runoff and evapotranspiration which is derived from precipitation falling in previous time intervals (called delayed runoff and evapotranspiration and signified by double primes). Thus

$$N = N' + N''$$

$$E = E' + E''$$

The parameterized form of equation (5) is

$$P - N' - E' = P' + N'' + E'' + \frac{\delta m}{\Delta t} \quad (6)$$

The respective terms are defined in terms of the six hydrologic parameters

$$\begin{aligned} N' &= n_p (P - P_n); & N'' &= vN^m \\ E' &= e_p (P - P_e); & E'' &= vE^m \end{aligned} \quad (7)$$

where n_p and e_p are dimensionless coefficients between 0 and 1 which determine the fraction of the precipitation in excess of the thresholds P_n and P_e that actually run off, and vN and vE are coefficients with units of reciprocal time which describe how frequently the stored soil water will be exchanged during the time interval Δt . The value of vN and vE will be greater than 0 and usually but not necessarily less than 1.

Lettau derives a differential equation for soil moisture from these ideas which, when integrated in a stepwise forward manner, yields

$$m_{i+1} = (P - N' - E')/v_j + (m_i - (P - N' - E;)/v_j) \exp(-v_j \Delta t) \quad (8)$$

where m_i is the stored exchangeable soil water of the beginning of the j th time interval,

$$v_j = vN_j + vE_j$$

From this time series of exchangeable soil moisture one may then calculate evapotranspiration and runoff according to equation 7.

The parameters may be modified in various ways to improve the representation

of the physical processes. vN may be a function of soil moisture. The two evaporation coefficients e_p and vE are likely to be functions of absorbed solar radiation. This introduces the need to include albedo, which may change with seasons and/or be a function of soil moisture. Further n_p or Pn may be made functions of soil moisture.

The Lettau model may be used as an independent test of the Thornthwaite water budget calculations of evapotranspiration and soil moisture. However, this will require knowing the six parameters, as functions of time if necessary, that describe the hydrologic behavior of stream basins for which good measurements of runoff, precipitation, and absorbed solar-radiation are known. It also requires developing an algorithm for determining the set of six parameters that best fit the hydrologic regime of a particular stream basin.

Finding a coherent set of parameter values which will allow the model to describe the hydrologic behavior of a particular river basin is called calibrating the model. This could be accomplished unambiguously if we knew the four time series of immediate and delayed runoff and immediate and delayed evapotranspiration. The time series of soil moisture storage could be substituted for one of the delayed process series. If the time series of precipitation, absorbed solar radiation, and runoff are known or estimable for a particular basin, it is possible to obtain sets of parameters which permit calculating the unknown time series. (Lettau and Baradas, 1973; Grangier, 1976, 1983).

The time series of immediate and delayed runoff (N' and N'') can be obtained from a stream gage record of discharge. Several approximation procedures have been used. However, for this work a more accurate procedure has been developed. The new computerized procedure uses the daily discharge and precipitation record

over a period of years to calculate the immediate runoff following a single or group of precipitation events which is then aggregated into monthly sums. The new method produces a reliable partitioning for the data examined in this study. Having obtained N' and N'' by differencing, the parameters describing them can later be obtained when the rest of the analysis is completed.

The two evaporative time series remain unknown, as do the series of soil moisture m_i and Δm_i . However, if we assume $\sum \Delta m_i = 0$ we can obtain the total evapotranspiration from the difference of the precipitation and runoff sums. This amount must be partitioned between immediate and delayed processes. Lettau and Baradas suggest a method of estimating a physically plausible guess for the immediate evaporation, e^* , which is used here. They then obtain time series of E'' and m_i by a successive approximation routine which uses the time series of N'' to improve the estimates. The routine converges very quickly. In the case of their tropical data, the resulting values of E'' and m_i are plausible. The retentivity, v , is found to be a function of m_i . When this method is applied to the data from New Jersey, the result is not satisfactory because the calculated soil moisture and m_i series show no seasonality. It appears that their procedure works when the seasonality is in the precipitation regime but not when the seasonality is in the solar radiation (temperature) regime, as in a temperate climate.

An alternative separation procedure is required which will produce the observed evaporation and soil moisture seasonal patterns. Such a procedure cannot be based solely on the seasonal march of absorbed solar radiation because that change is not large enough (here about 3.6:1) to account for the seasonal variation in evapotranspiration (5:1). It appears that the phenological cycle of the vegetation actively regulates the evapotranspiration.

Several procedures to obtain E'' were tried, none really satisfactory. The one presented here is preferred to the others because of its similarity to Lettau's approach which is based on the premise that a solution has been found if the chosen parameter values reveal a regular functional relationship between model soil moisture and the delayed process parameters.

The approach of Lettau and Baradas was modified to assert that the delayed evapotranspiration be proportional to the normalized solar radiation, the soil moisture, and a new factor α which describes the relative effectiveness of the vegetation in transpiring. A value of 1 is applied for the months of full vegetation development, June, July, August and September. A value of .1 is applied in December, January and February; .2 for March and November; and .7 for May and October. Alpha (α) is applied only to the delayed evaporation during the calibration procedure. It implies the assumption that vegetation is responsible for the delayed evapotranspiration, while the immediate evapotranspiration proceeds independently of the stage of the vegetation.

Round #1

v^I assigned by operator

$$U_*^I = \frac{\Sigma E'' - \Sigma N''}{\Sigma E'' + \Sigma N''}$$

ORIGINAL PAGE IS
OF POOR QUALITY

where $\Sigma E'' = \Sigma P - \Sigma N - \Sigma E'$

$$m_i^I = e^{-\tau} (m_i + \int e^{+\tau} \cdot \left(\frac{P - N' - E'}{v^I} \right) d\tau)$$

$$E''^I = \frac{\alpha_i \left(\frac{F_i}{E} \right) m_i^I}{\Sigma \alpha_i \left(\frac{F_i}{E} \right) m_i^I} \cdot \Sigma E''$$

where $\Sigma E'' = \Sigma P - \Sigma N - \Sigma E'$

$$N''^I_{\text{calc}} = \frac{1 - U_*^I}{2} v^I m_i^I$$

Round #2

$$v_i^{II} = \frac{N''_{\text{obs}} + E_i^{II}}{m_i^I}$$

$$U_*^{II} = \frac{E''^I - N''_{\text{obs}}}{E''^I + N''_{\text{obs}}}$$

$$m_i^{II} = e^{-\tau} (m_i + \int e^{+\tau} \cdot \left(\frac{P - N' - E'}{v^{II}} \right) d\tau)$$

$$E''^{II} = \frac{\alpha_i \left(\frac{F_i}{E} \right) m_i^{II}}{\Sigma \alpha_i \left(\frac{F_i}{E} \right) m_i^{II}} * \Sigma E''$$

$$N''^{II}_{\text{calc}} = \frac{1 - U_*^{II}}{2} v_i^{II} m_i^{II}$$

Note that the soil moisture series may be calculated numerically, by forward integration, according to Lettau's solution (eq. 8)

The iteration is continued, with the observed delayed runoff being used to revise the time series of the partitioning parameter u^* and v_i until the calculated values of N'' equal the observed values of N'' . Closure occurs within three or four rounds. The results of using this procedure on the data for the Maurice River in New Jersey will illustrate the type of result which can be achieved.

The Maurice River in southern New Jersey has a drainage area of about 100 square miles, of which 48% is agricultural land, 29% oak-pine forest, 20% hardwood swamp forest, and 1% each broad leaf upland forest, urban land, and open water. The soils for 85% of the area are graveley and sandy, and are well drained. The terrain is gently sloping coastal plane. A weighted average for the water holding capacity of the soils lies between a low of .1 and a high of .17 per cm of top soil. The river is dammed at Norma, where the stream gage is located. A lake and marshes extend upstream from the dam.

Daily precipitation for Clayton, located in the center of the basin, was used. (Data from other surrounding stations were used in monthly analysis only). The daily gaged runoff for the years 1949-1962 was separated into immediate and delayed runoff by the routine described previously. Monthly solar radiation was obtained from the Seabrook station, about 12 miles distant, for most of the period. Missing months were estimated from a regression on an average of New York City and Washington, the coefficient of determination for which against Seabrook is .982. Albedo for the basin was obtained as a weighted average of values obtained from the literature for such land uses and seasons. The principle reference used was Kung, Bryson, and Lenschow (1964). The region has relatively mild winters with average monthly temperatures only infrequently below freezing. Snow rarely lingers longer than five days. The soil may freeze if snow does not accompany the cold.

The years 1949-1962 were divided into years of below average precipitation (dry) and years of above average precipitation (wet) for separate processing. The data and analysis for wet, dry and all years are given below. (Tables 1 and 2) Figures 1 and 2 are the plots of the hydrologic data used in attempting to calibrate the model. There appears no reason for uncertainty in the separation of total runoff into immediate and delayed runoff. Figure 3 and 4 are the graphic output of the interactive microcomputer program which is my implementation of a calibrating algorithm. For the case illustrated, the total flushing frequency v was initially set to .25 for both wet and dry years and e^* (HE) is .15. Figure 3 is a plot of the monthly values of $v_N = N''_{obs}/i$ obtained after convergence (W for wet years and D for dry years). Notably, v_N appears to be independent of soil moisture. This result is a consequence of the procedural assumption for separating out E'' . Further, there is considerable scatter of points which probably is also an artifact of forcing all of the soil moisture dependence onto E'' . Figure 4 is a plot of normalized E'' against the soil moisture where normalized $E'' = E''/\alpha \frac{F_1}{E}$. In this case the linear plot is forced by the procedure and does not reveal anything about the quality of the fit produced by the selected parameters. Ideally, these two plots would reveal the best fitting set of parameter values by showing a tendency toward smooth functions as the proper parameter values are chosen. In these runs there were no clear trends toward functional relations, so it is not possible to choose proper values for e^* and v except to assert that they each probably lie within the range of .15 to .3.

Figure 5 shows a plot of the calculated value of the total evapotranspiration in two cases, that where $v = .15$ and $e^* = .15$ and where $v = .25$ and $e^* = .25$. Values of actual evapotranspiration calculated according to the Thornthwaite model for the years 1950-1956, with storage 225 mm are also given for comparison.

An examination of the three evapotranspiration plots in figure 5 reveals first that the two Lettau models show very little difference in the amount and timing of the total evapotranspiration. The model with the larger flushing rate and larger immediate evaporicity shows a small tendency for larger evapotranspiration early and late in the year and a slightly lower peak in June. Both show the strong dependence on absorbed solar radiation, which reaches its maximum value in June. Total evapotranspiration then falls rather rapidly as the soil moisture is drawn down and the absorbed solar radiation diminishes. The Thornthwaite model actual evapotranspiration shows considerably less water loss in the winter and spring, peaks in July and continues to show higher evapotranspiration than the Lettau model until December. The timing of the water loss is shifted according to this model's dependence on air temperature.

There is no clear basis for choosing between these two models. The factor α used in the Lettau model could be adjusted to change the seasonal timing toward that of the Thornthwaite model. However, the values actually used were chosen according to estimates of the state of vegetation development in each month (see Tables 1 and 2), and should be changed only on the basis of better objective information about the relative seasonal transpirational effectiveness of the vegetation.

There is a need to devise a better procedure for obtaining the Lettau delayed evapotranspiration in climates such as this where the seasonality is driven by the available energy and not by the precipitation. Until then a precise basin calibration for seasonal cycles cannot be done.

Table 1
 Maurice River
 Average Years
 1949-1962

MAURCLAY	AVG YEARS	MU= .25	ME= .15	FE=N'	NUMBER OF ITERATIONS: 4							
SUMS:												
PRECIPITATION	1190				RUNOFF= 521							
IMMEDIATE EVAPORATION	162				DELAYED EVAPORATION 507							
IMMEDIATE RUNOFF	148				DELAYED RUNOFF 374							
PRECIPITATION	90	95	124	97	99	87	112	121	105	86	86	90
RUNOFF	50	52	66	59	51	36	31	34	33	30	38	43
IMMEDIATE RUNOFF	14	17	25	13	5	4	7	13	12	7	14	16
DELAYED RUNOFF	35	35	41	46	46	32	24	21	21	23	23	27
IMMEDIATE EVAPORATION	5	8	14	15	20	19	23	21	16	10	6	5
ABSORBED SOLAR RAD	173	196	280	353	414	452	435	387	333	240	164	125
LY/DAY												
SOIL MOISTURE	334	364	392	390	349	288	244	231	228	235	261	299
SMOISAV	301.244											
MU	0.1169	0.1104	0.1482	0.2527	0.3548	0.4590	0.4327	0.3900	0.3496	0.2270	0.1144	0.1004
MUAV	.254675											
MUM	0.1062	0.0952	0.1050	0.1166	0.1310	0.1104	0.0970	0.0914	0.0929	0.0972	0.0891	0.0908
USTAK	-0.8172	-0.7256	-0.4171	0.0770	0.2614	0.5192	0.5517	0.5315	0.4683	0.1437	-0.5575	-0.8081
USTAKAV	-0.643963											
DELAYED EVAPORATION	4	6	17	53	78	100	82	69	59	31	7	3
NORMALIZED DELAYED EVAP	0.2573	0.2807	0.3027	0.3007	0.2690	0.2223	0.1879	0.1780	0.1760	0.1815	0.2015	0.2304
ALBEDO	.160	.160	.140	.140	.140	.150	.150	.150	.150	.140	.140	.160
ALPHA	0.1	0.1	0.2	0.5	0.7	1.0	1.0	1.0	1.0	0.7	0.2	0.1
CALC DELRO	35	35	41	45	46	32	24	21	21	23	23	27
TOTAL EVAPOTRANSPIRATION	9	13	31	68	78	120	105	90	74	40	13	8

Table 2 Maui, 2/ver 1949-1962
Wet years

ORIGINAL PAGE 5
OF POOR QUALITY

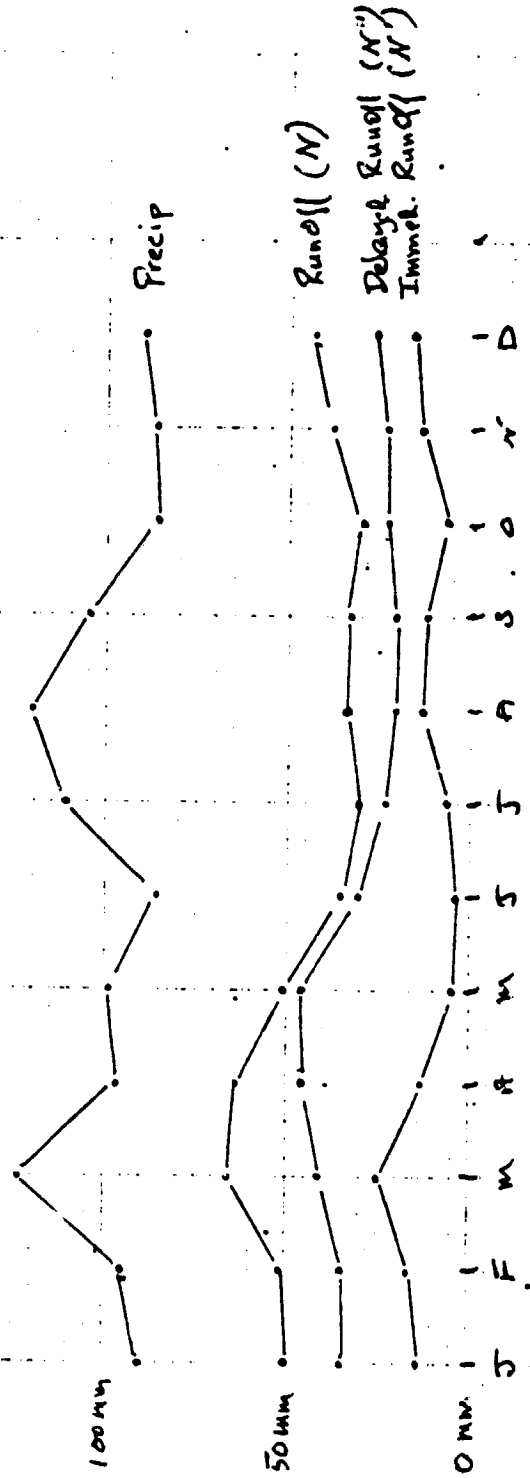
Dry years

MAURCLAY WET YEARS			MAURCLAY DRY YEARS		
MU=	HE=	PE=N'	MU=	HE=	PE=N'
SUNS:		NUMBER OF ITERATIONS: 4	SUNS:		NUMBER OF ITERATIONS: 4
PRECIPITATION 1374	RUNOFF= 594		PRECIPITATION 1033	RUNOFF= 459	
IMMEDIATE EVAPORATION 189	DELAYED EVAPORATION 591		IMMEDIATE EVAPORATION 139	DELAYED EVAPORATION 435	
IMMEDIATE RUNOFF 149	DELAYED RUNOFF 446		IMMEDIATE RUNOFF 147	DELAYED RUNOFF 312	
PRECIPITATION 116	159	111	121	113	136
RUNOFF 51	72	48	61	43	41
IMMEDIATE RUNOFF 12	14	25	12	6	4
DELAYED RUNOFF 39	39	48	55	40	29
IMMEDIATE EVAPORATION 7	10	19	18	24	25
ABSORBED SOLAR RAD LY/DAY 137	210	280	349	418	451
SOIL MOISTURE 379	426	469	474	427	360
SMOISAV 354.127					
MU	0.1128	0.1080	0.1429	0.2460	0.5454
MUAV	.251639				
MUM	0.1026	0.0925	0.1015	0.1188	0.1104
USTAR	-0.8197	-0.7122	-0.4204	0.0421	0.2537
USTARAV	-0.083559				
DELAYED EVAPORATION 4	7	19	61	92	120
NORMALIZED DELAYED EVAP	0.2809	0.3151	0.2175	0.3511	0.3162
ALBEDO 160	.160	.140	.140	.150	.150
ALPHA 0.1	0.1	0.2	0.5	0.7	1.0
CALC DELRO 39	39	48	56	55	40
TOTAL EVAPOTRANSPIRATION 11	17	39	79	117	145
PRECIPITATION 116	109	159	111	121	113
RUNOFF 51	53	72	48	61	43
IMMEDIATE RUNOFF 16	20	25	15	5	4
DELAYED RUNOFF 32	31	36	36	3	25
IMMEDIATE EVAPORATION 4	6	10	13	16	14
ABSORBED SOLAR RAD LY/DAY 139	185	280	356	411	453
SOIL MOISTURE 294	311	326	317	282	227
SMOISAV 256.036					
MU	0.1214	0.1134	0.1548	0.2577	0.3668
MUAV	.258981				
MUM	0.1101	0.0985	0.1055	0.1138	0.1338
USTAR	-0.8142	-0.7368	-0.4143	0.1169	0.2706
USTARAV	-0.0466016				
DELAYED EVAPORATION 3	5	15	46	66	83
NORMALIZED DELAYED EVAP	0.2380	0.2515	0.2538	0.2568	0.2280
ALBEDO 160	.160	.140	.140	.140	.150
ALPHA 0.1	0.1	0.2	0.5	0.7	1.0
CALC DELRO 32	31	36	36	38	25
TOTAL EVAPOTRANSPIRATION 7	11	25	58	82	97

71 64 8
28 31 37
8 10 12
20 21 20
8 5 4
237 169 125
224 238 26
0.2238 0.1157 0.09
0.0819 0.0898 0.0847
0.5232 0.1975 -0.5284 -0.77
54 30 6
0.1508 0.1669 0.1813 0.1926 0.21
0.150 0.150 0.150 0.150 0.150
0.2 0.2 0.1
17 20 21
77 74 58 11

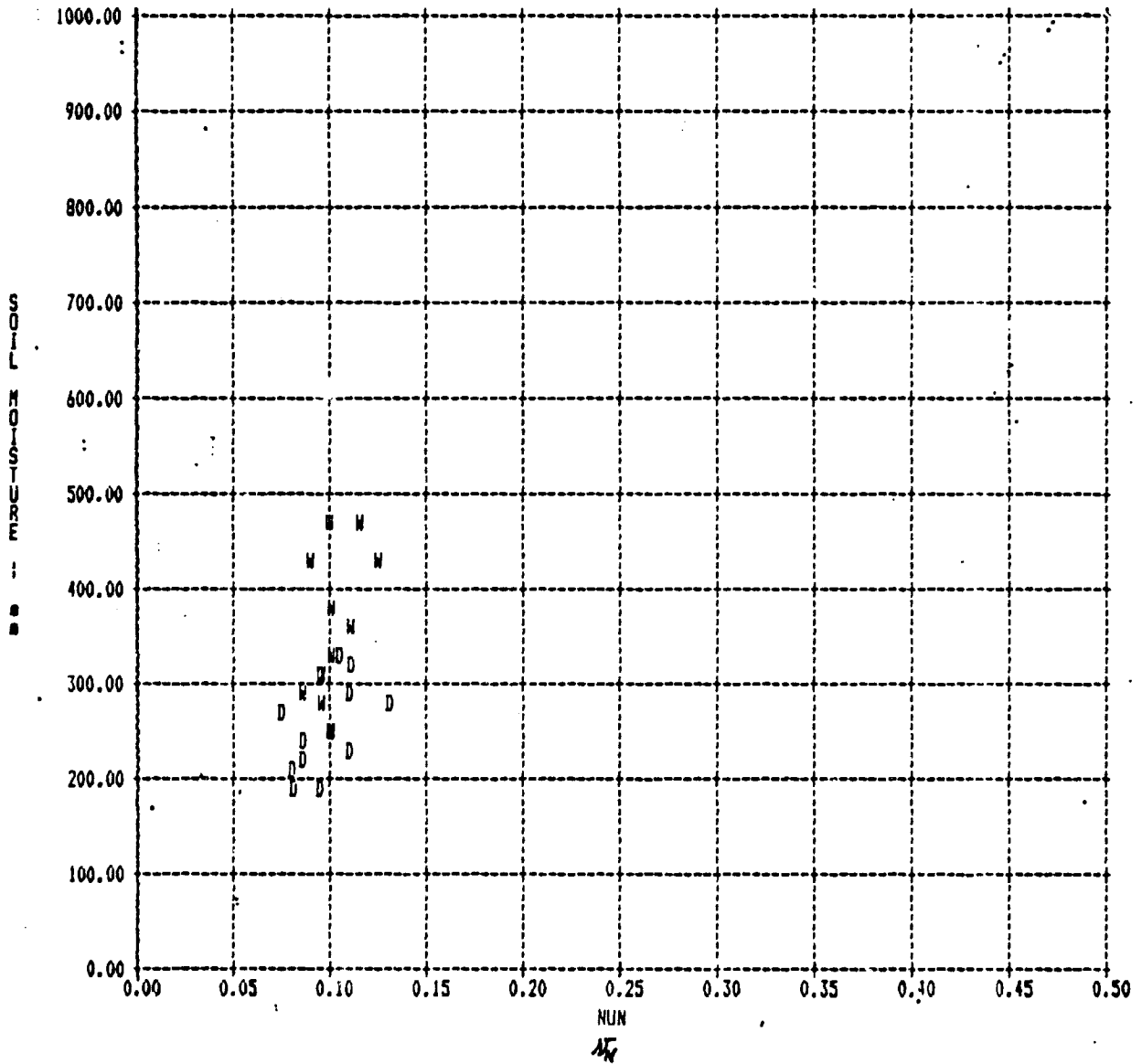
Figure 1

Maurice River, NS
1949-1961
Average Years



ORIGINAL PAGE IS
OF POOR QUALITY

MAURCLAY NU= .25 HE= .15



ORIGINAL PAGE IS
OF POOR QUALITY

MAURCLAY NU= .25 HE= .15

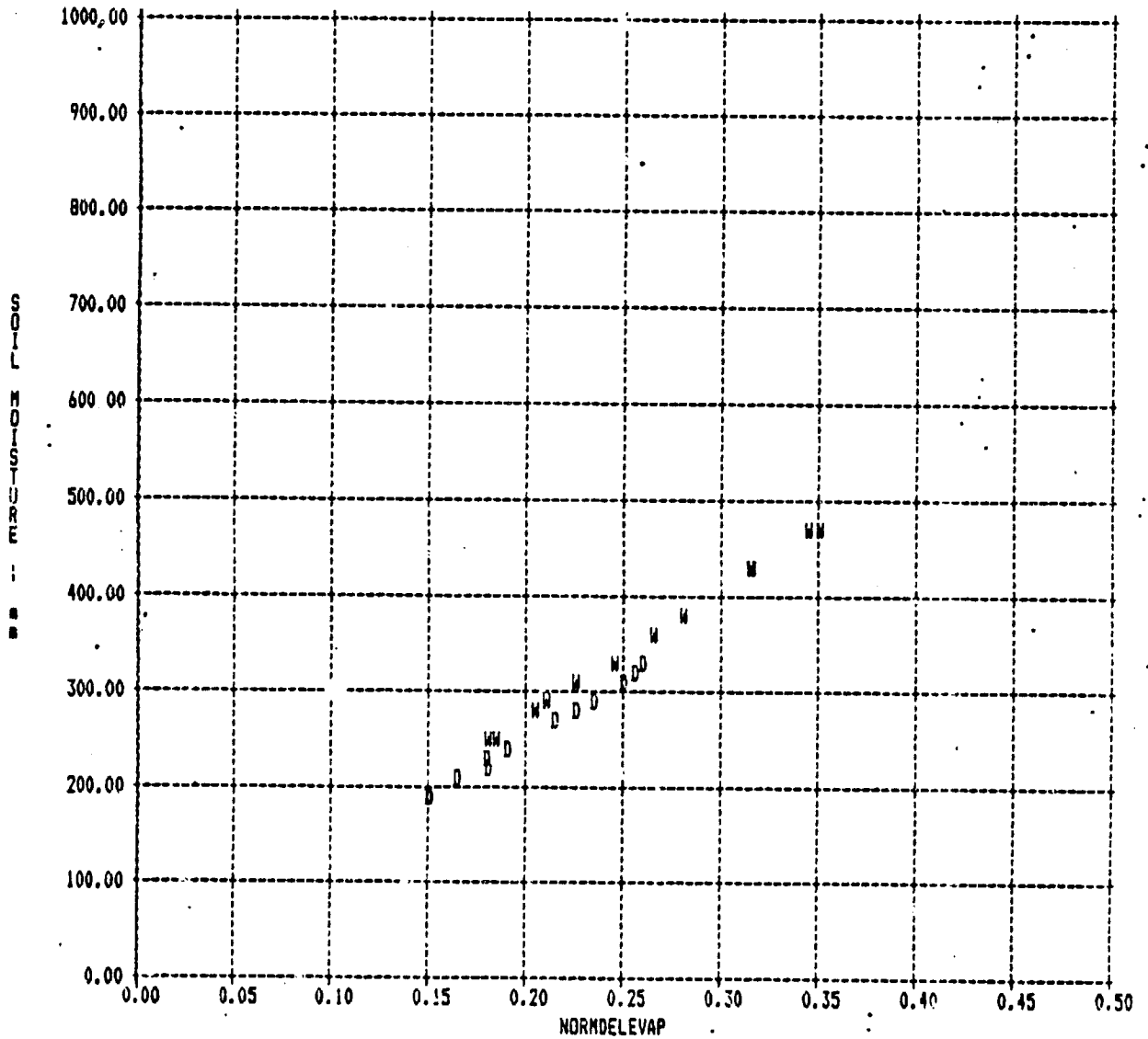


FIGURE 5

Maurice River, NJ
 1949-1961
 Average years

Evapotranspiration
 $X = 1.15$
 $O = 1.25$
 $n = 11$ months

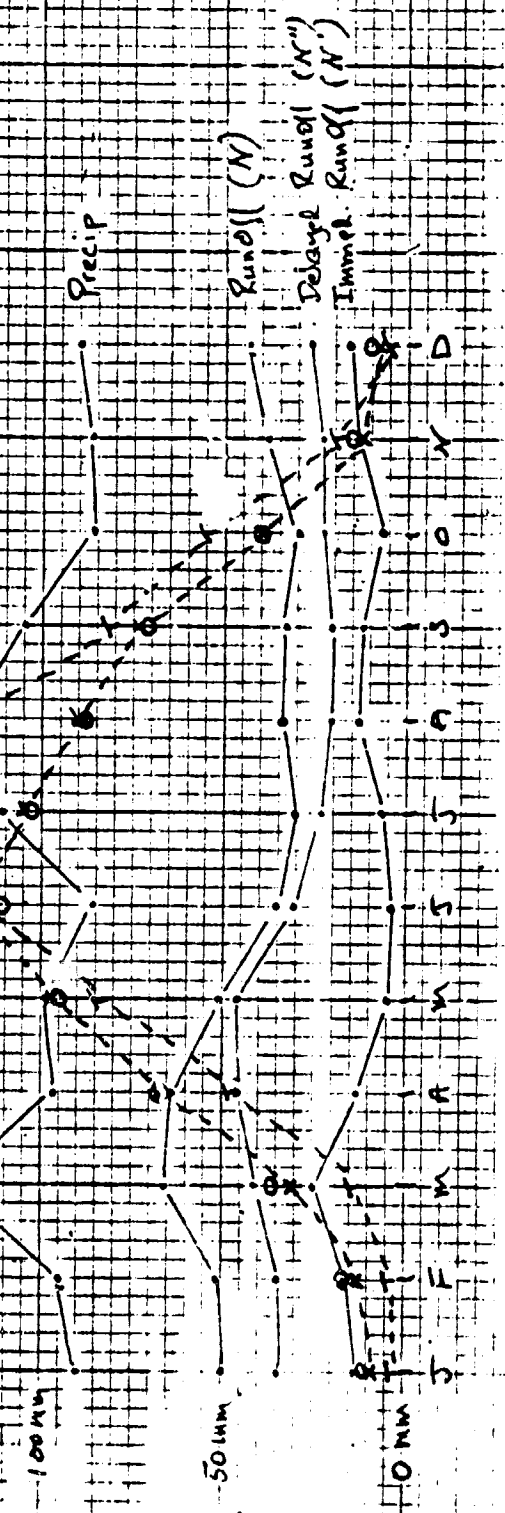


Figure 5

Maurice River, NJ
1949-1961
Average Years

Evapotranspiration
 $X = \dots$
 $N = .15$
 $N = .25$
 $T = \dots$

